Economic Geology, v. 114, no. 1, pp. 47–66

Lead Isotope Geochemistry of Shales from the Wolverine Volcanogenic Massive Sulfide Deposit, Yukon: Implications for Pb Isotope Vectoring in Exhalative Ore Systems

Stephen J. Piercey[1,†] and Balz S. Kamber[2,*]

[1] *Department of Earth Sciences, Memorial University, St. John's, Newfoundland and Labrador A1B 3X5, Canada*

[2] *Irish Centre for Research in Applied Geosciences (iCRAG), Department of Geology, Trinity College Dublin, Dublin 2, D02 PN40, Ireland*

Abstract

Combined whole-rock lead isotope and high-precision trace element data are reported for shales from the Wolverine deposit and surrounding prospects (e.g., Puck, Fisher, Sable) to elucidate the source of Pb in the shales and their potential utility as an exploration vector. Shales exhibit distinct variations in time-integrated U/Th/Pb evolution with proximity to mineralization. Distal samples resemble the local crustal Pb isotope composition of the northern Cordilleran continental crust (i.e., shale curve). More proximal samples exhibit evidence for hydrothermal activity, but were not significantly mineralized. They have very high U/Th and U/Pb and anomalous present-day $^{206}Pb/^{204}Pb$ (>20) coincident with elevated Y/Ho, Zr/Hf, and carbonate alteration. These signatures were derived from oxygenated seawater and imprinted on the shales by oxygenated, CO_2-rich hydrothermal fluids that contained uranyl carbonate ions (e.g., $UO_2(CO_3)_3^{4-}$). It is envisioned that this was due to shallow-level (within 50 m of the seafloor), near-vent ingress of oxygenated seawater associated with hydrothermal venting. A third population of samples is most proximal to mineralization. These, too, have trace element signatures (i.e., high Y/Ho, Zr/Hf, CO_2-U enrichment) inherited from seawater, but they do not exhibit anomalous present-day $^{206}Pb/^{204}Pb$, being more juvenile in $^{206}Pb/^{204}Pb$, $^{207}Pb/^{204}Pb$, and $^{208}Pb/^{204}Pb$. This isotope composition coincides with enrichments in Pb, Zn, Cu, Tl, Sb, W, and Sn (±Cu, Mo). The Pb enrichment associated with mineralization effectively buffered these samples from appreciable Pb isotope evolution, despite overprinting by uranyl carbonate. The juvenile Pb associated with the shales proximal to mineralization argues for deep-penetrative circulation of hydrothermal fluids and leaching of Pb from mafic igneous rocks at depth and/or influence from juvenile magmas at depth (i.e., magmatic fluids). Both of these processes were likely critical for the genesis of mineralization at Wolverine.

This study illustrates the utility of quadrupole inductively coupled plasma-mass spectrometry (ICP-MS) for providing sufficiently precise and accurate Pb isotope determinations for district-scale metallogenic evaluations. Furthermore, the coupling of solution ICP-MS Pb isotopes with high-precision trace element geochemistry from the same digest provides a powerful tool for regional exploration studies for hydrothermal mineralization in shale basins.

Introduction

Common Pb isotopes provide a critical tool in understanding the origin of Pb in mineral deposits and their host terranes (Gulson, 1986; Tosdal et al., 1999). Lead isotopes have been particularly useful in the tracing of Pb in sulfide minerals in volcanogenic massive sulfide (VMS) and sediment-hosted Zn-Pb deposits (e.g., Franklin and Thorpe, 1982; Godwin and Sinclair, 1982; Swinden and Thorpe, 1984; Marcoux, 1997; Thorpe, 1999; Ayuso et al., 2004; Mortensen et al., 2006, 2008; Layton-Matthews et al., 2013). However, in most of these studies the focus has been on sulfide minerals directly associated with mineralization, with very few studies on the immediate host rocks to mineralization (Ayuso and Schulz, 2003). Even fewer have been undertaken on shales associated with mineralization (Gulson, 1976; Turner and Kamber, 2012).

In this study, we build on the work of Piercey et al. (2016) and provide Pb isotope data for shales from the Wolverine VMS deposit. The shale samples are from various stratigraphic heights in the deposit and from both the deposit proper and other prospects along strike. The purpose of the study was to evaluate the sources of Pb in the shales within the deposit and to test the potential of Pb isotopes as an exploration tool in both the Wolverine basin and in other shale-associated VMS deposits. The results presented herein illustrate that Pb isotopes, when combined with trace element geochemistry, have significant utility for defining prospective versus less prospective shales and may have applications in other shale-rich environments and hydrothermal deposits globally (e.g., VMS, sedimentary exhalative, and Broken Hill-type deposits).

† Corresponding author: e-mail, spiercey@mun.ca

*Current address: School of Earth, Environmental and Biological Sciences, Queensland University of Technology, Brisbane, Queensland 4000, Australia.

Regional Geology

The Wolverine deposit is in the Finlayson Lake district of southwest Yukon, Canada, and consists of Devonian to Permian rocks of the Yukon-Tanana and Slide Mountain terranes (Fig. 1). These terranes represent a continental arc to back-arc rift that formed along the ancient Pacific margin of North America from the late Devonian to Permian (Nelson et al., 2006; Piercey et al., 2006). The rocks of the district are juxtaposed against the North American continental margin along the post-Late Triassic Inconnu thrust (Fig. 1; Murphy et al., 2006). Despite being deformed and metamorphosed, regionally extensive stratigraphic units have been defined with primary geologic features and geochemical signatures locally well preserved (e.g., Murphy et al., 2006; Piercey et al., 2006).

The district is subdivided into several informal fault- and unconformity-bounded groups and formations (Figs. 1, 2; Murphy et al., 2006). The lowermost package of the

ISSN 0361-0128; doi: 10.5382/econgeo.2019.4619; 20 p.
Digital appendices are available in the online Supplements section.

Submitted: May 27, 2017
Accepted: December 16, 2018

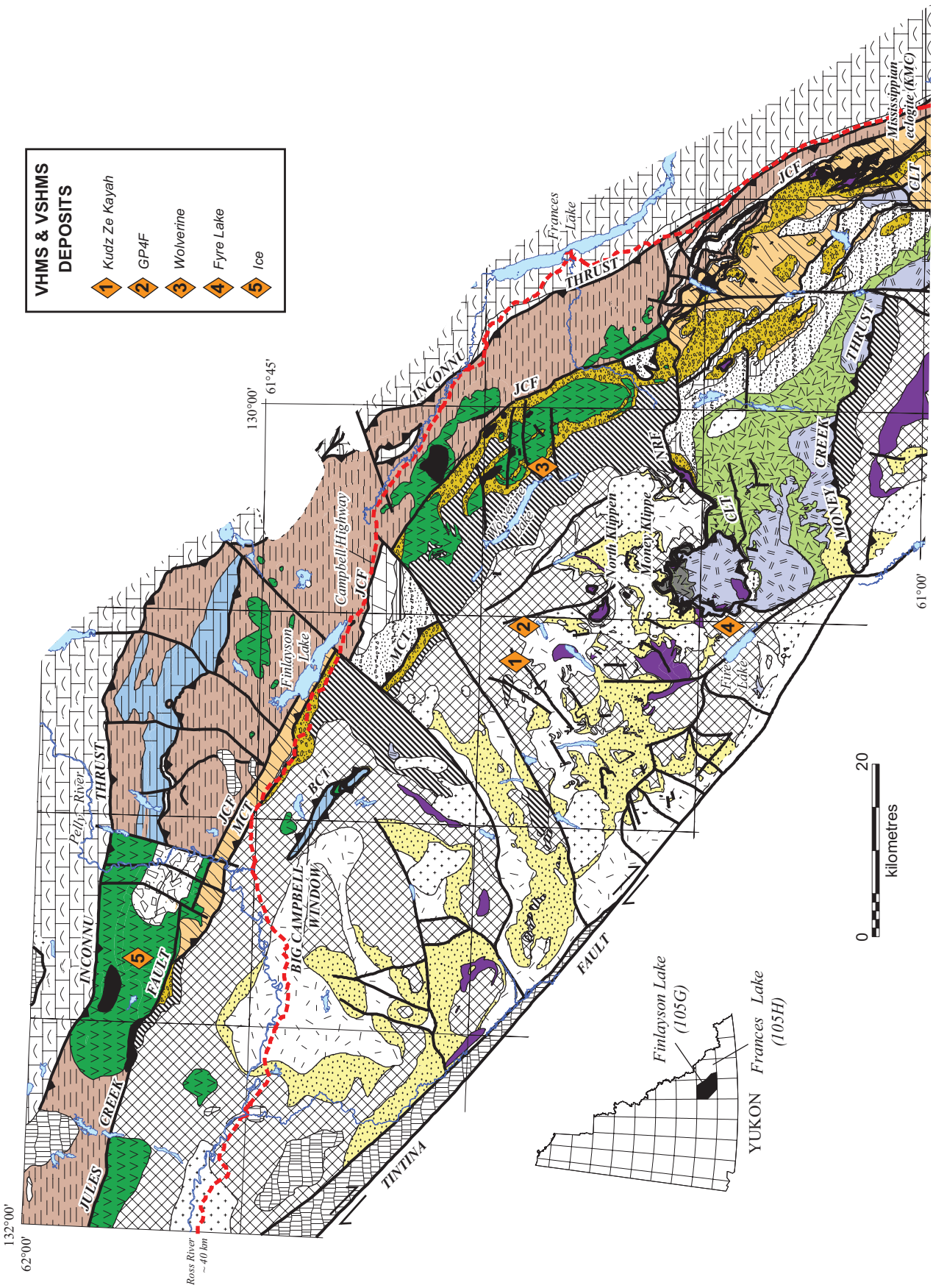

Fig. 1. Geologic map of the Finlayson Lake district with location of the VMS deposits (from Murphy et al., 2006). Abbreviations: CLT = Cleaver Lake thrust, JCF = Jules Creek fault, KMC = Klatsa metamorphic complex, MCT = Money Creek thrust, NRF = North River fault, SMT = Slide Mountain terrane, VHMS = volcanic-hosted massive sulfide, VSHMS = volcanic sediment-hosted massive sulfide, YTT = Yukon-Tanana terrane.

LEGEND

Mesozoic and Cenozoic


undifferentiated intrusions


undifferentiated volcanic rocks

NORTH AMERICAN CONTINENTAL MARGIN

Triassic


dark shale, siltstone and limestone

Paleozoic


undifferentiated formations of Selwyn Basin, McEvoy Platform, Earn Group and Mt. Christie Formation

POST - YTT / SMT AMALGAMATION

Triassic


gray shale, siltstone and limestone

Permian - Triassic

SIMPSON LAKE GROUP


polymictic conglomerate, sandstone, siltstone, mafic and felsic volcanic rocks, limestone

SLIDE MOUNTAIN TERRANE

INTRUSIVE ROCKS

Early Permian


ultramafic and mafic intrusions

LAYERED ROCKS

Lower to Middle Permian

Gatehouse Formation


limestone and quartzite

SLIDE MOUNTAIN TERRANE

Lower Permian

Campbell Range Formation


basalt and varicolored chert

Carboniferous to Permian?

FORTIN CREEK GROUP


dark phyllite and chert, varicolored chert, chert-pebble conglomerate, sandstone, limestone, felsic and mafic metavolcanic rocks

YUKON-TANANA TERRANE

INTRUSIVE ROCKS

Late Devonian to Early Mississippian

SIMPSON RANGE PLUTONIC SUITE


granite, quartz monzonite, granodiorite

GRASS LAKES PLUTONIC SUITE


granite, quartz monzonite augen granite


ultramafic and mafic intrusions, Big Campbell and Cleaver Lake thrust sheets

LAYERED ROCKS

Lower Permian

Money Creek Formation


dark phyllite and sandstone, chert, chert-pebble conglomerate, diamictite

Mid-Pennsylvanian to Lower Permian

Finlayson Creek limestone


massive bioclastic limestone

YUKON-TANANA TERRANE

Upper Mississippian to mid-Pennsylvanian

undifferentiated White Lake and King Arctic formations


green and pink chert, limestone, sandstone, conglomerate, mafic metavolcanic rocks

Upper Mississippian

Whitefish limestone


massive bioclastic limestone

Lower Mississippian

Tuchitua River Formation


intermediate, felsic and mafic volcanic rocks, sandstone, chert, limestone

WOLVERINE LAKE GROUP


undifferentiated mafic and felsic volcanic rocks and dark clastic rocks

Upper Devonian to Lower Mississippian

Cleaver Lake Formation


calc-alkaline basalt, rhyolite, chert and volcanic-derived sandstone

Waters Creek Formation


felsic to intermediate metavolcanic rocks and carbonaceous phyllite

GRASS LAKES GROUP


undifferentiated mafic and felsic volcanic rocks and dark clastic rocks of the Fire Lake, Kudz Ze Kayah and Wind Lake formations

Pre-Upper Devonian

North River Formation


quartzose metaclastic rocks, marble and non-carbonaceous pelitic schist

Fig. 1. *(Cont.)*

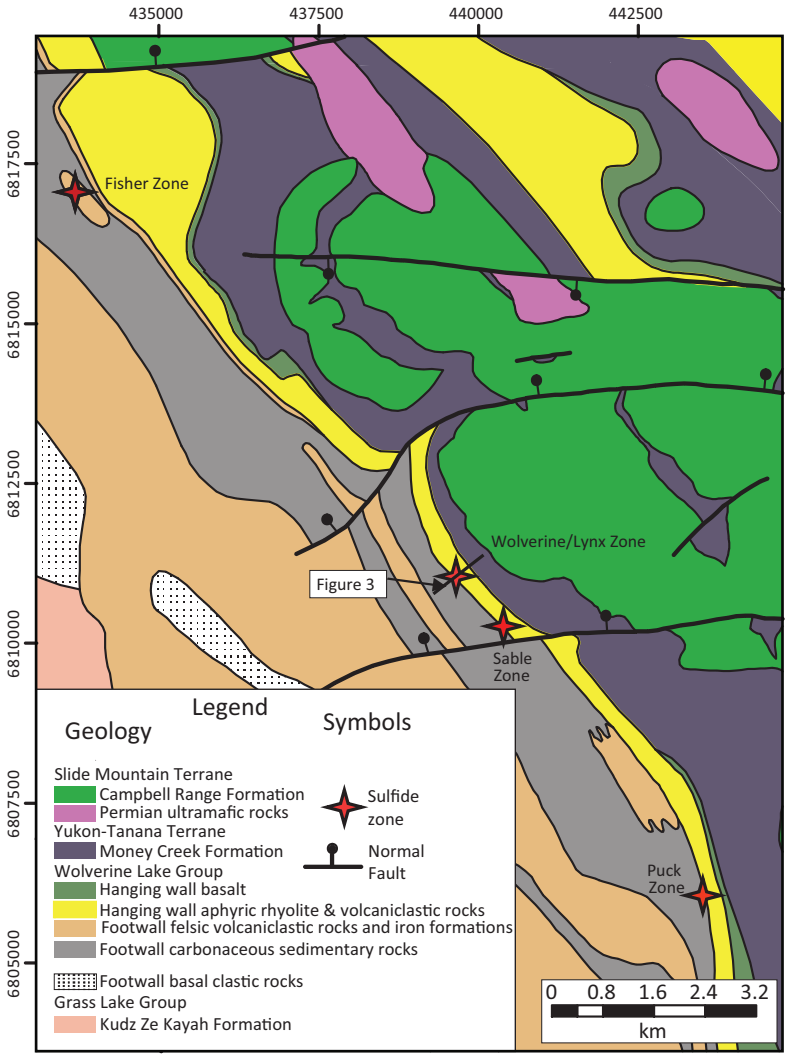

Fig. 2. Geology of the immediate Wolverine deposit area, showing the locations of different zones of the Wolverine deposit. Geology from Murphy et al. (2006).

Yukon-Tanana terrane is found in the footwall of the Money Creek thrust (Fig. 1; Murphy et al., 2006) and consists of mafic and felsic metavolcanic and metasedimentary rocks of Upper Devonian and older Grass Lakes Group, Late Devonian to early Mississippian granitic metaplutonic rocks of the Grass Lakes plutonic suite, and metasedimentary and mafic and felsic metavolcanic rocks of the unconformably overlying lower Mississippian Wolverine Lake Group (Figs. 1, 2). The Grass Lakes Group is host to the Fyre Lake, Kudz Ze Kayah, and GP4F deposits, whereas the Wolverine Lake Group hosts the Wolverine deposit (Figs. 1, 2). The Grass Lakes and Wolverine Lake groups have been interpreted to represent a continental back-arc rift to back-arc basin assemblage (Piercey et al., 2001a, b, 2004, 2006; Murphy et al., 2006).

The hanging wall of the Money Creek thrust consists of Upper Devonian to lower Mississippian metasedimentary and felsic to intermediate metavolcanic rocks and granitoid rocks (Mortensen, 1992), Lower Permian limestone, and, locally, Lower Permian dark gray basinal clastic rocks (Fig. 1). These latter rocks are overlain by rocks of an upper thrust sheet that comprises undeformed, predominantly mafic Late Devonian volcanic rocks of the Cleaver Lake Formation, spatially associated and probably comagmatic felsic, mafic, and ultramafic metaplutonic rocks, and a crosscutting early Mississippian pluton of the Simpson Range plutonic suite (Fig. 1). None of these rock units host significant VMS mineralization. The rocks of the hanging wall of the Money Creek thrust (Cleaver Lake Formation and Simpson Range plutonic suite) have been interpreted to represent magmatism within a continental arc (Grant, 1997; Piercey et al., 2001b, 2003, 2006; Murphy et al., 2006).

To the north and east, the imbricated rocks of the Yukon-Tanana terrane are juxtaposed against rocks of the Slide Mountain terrane along the Jules Creek fault (Fig. 1). In this area, the Slide Mountain terrane comprises the Mississippian to Lower Permian Fortin Creek Group metasedimentary and metavolcanic rocks. The Slide Mountain terrane also includes pristine to weakly foliated Lower Permian basalt, mafic and ultramafic plutonic rocks, and minor sedimentary rocks of the Campbell Range Formation. The mafic rocks of the Slide Mountain terrane are host to the Ice VMS deposit (Fig. 1) and are interpreted to have formed in a Permian back-arc basin

environment (Plint and Gordon, 1997; Piercey et al., 2006, 2012).

Wolverine Deposit Stratigraphy and Shale Relationships

The geology of the Wolverine deposit, mineralization, and associated shales has been documented in greater detail in Piercey et al. (2016) and is synthesized here. The deposit footwall consists of shales interlayered with felsic volcaniclastic rocks that are crosscut by ~352 to 347 Ma feldspar- and quartz-feldspar porphyry intrusions (Bradshaw, 2003; Bradshaw et al., 2008; Piercey et al., 2008). The hanging wall to the deposit consists of interlayered shale, carbonate exhalite, iron formation, silica-pyrite exhalite, aphyric rhyolite siltstone/tuff, rhyolite siltstone breccia, graywacke, and mafic volcanic and intrusive rocks (Figs. 2, 3; Bradshaw et al., 2008). Shales occur at various stratigraphic levels including the deeper footwall, immediately on the mineralized horizon, interlayered with

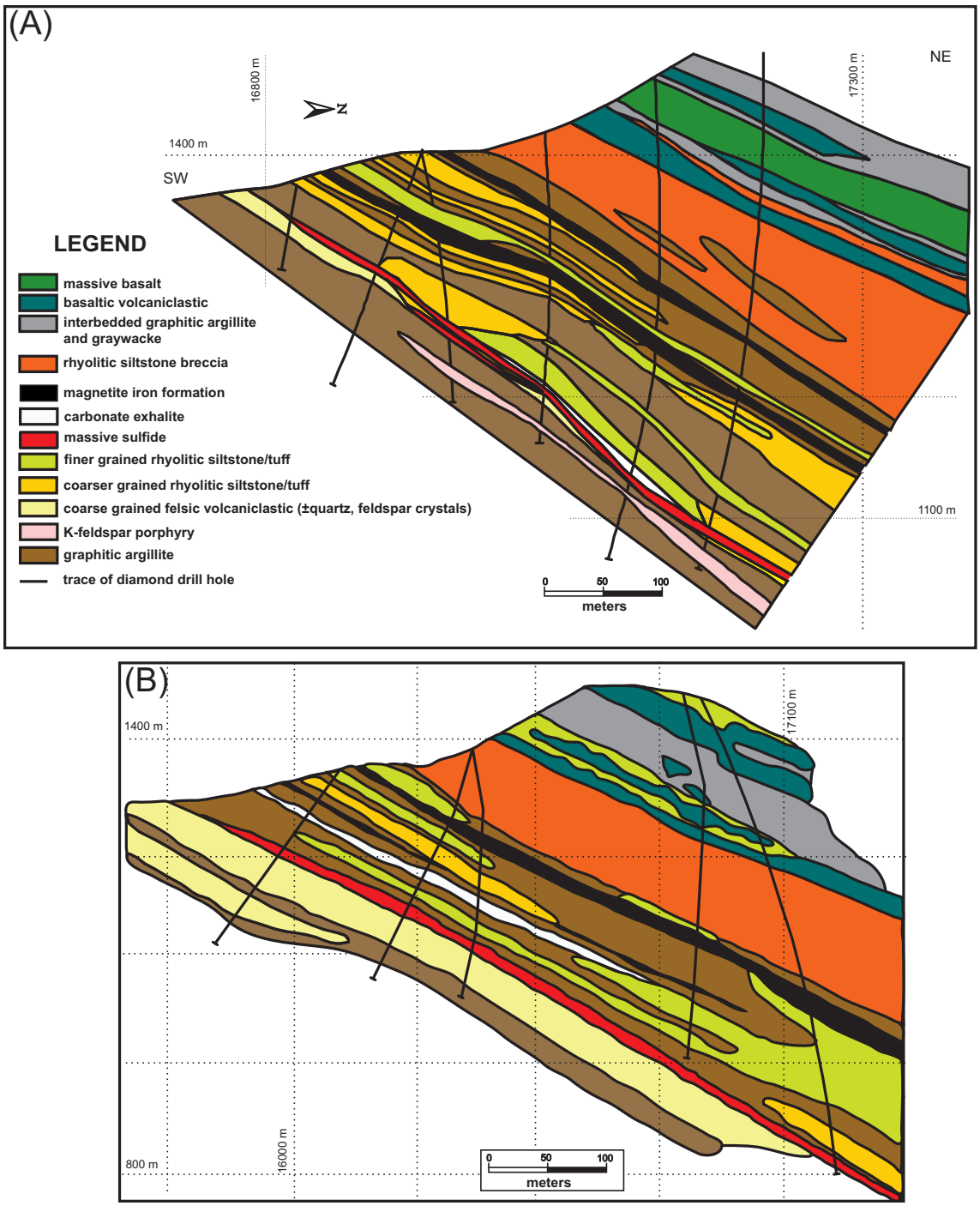

Fig. 3. Geologic cross sections through the Lynx (A) and Wolverine (B) zones of the Wolverine deposit. Locations of cross sections in the deposit are shown in Figure 2. Sections modified from Bradshaw (2003) and Bradshaw et al. (2008).

the hanging wall stratigraphy between the mineralization and the uppermost iron formation, and in the uppermost hanging wall above the iron formations (Figs. 2, 3).

Along strike, there are other mineralized zones with stratigraphy similar to that of the Wolverine deposit, but they have only minor mineralization (Fig. 2). The Fisher zone contains a hanging wall and footwall similar to those of the Wolverine deposit, and has minor intersections of sericite- to chlorite-altered footwall felsic tuffaceous rocks with narrow bands of sphalerite-pyrite-galena and thick, fold-repeated iron formation (Peter et al., 2007). Shales are associated with the immediate footwall tuffaceous rocks, and some of the drill holes at Wolverine extend very deep into the footwall (100s of meters) and thus provide shales from the deepest parts of the Wolverine deposit. In the hanging wall of the Fisher zone, shales are interlayered with volcanic siltstones, carbonate exhalite, volcanic breccias, and uppermost hanging-wall stratigraphy, similar to the Wolverine deposit proper.

The Sable zone occurs 1.6 km along strike from the Wolverine deposit and is stratigraphically similar to the Wolverine deposit (Fig. 2). It contains footwall felsic volcaniclastic rocks interlayered with carbonaceous shales, and also contains ~352 Ma quartz-K-feldspar porphyry intrusions (Piercey et al., 2008). Mineralization consists of thin intersections of massive sulfide with strong quartz-pyrite-Fe carbonate alteration (Peter et al., 2007). The hanging wall to mineralization consists of abundant volcanic siltstone interlayered with carbonaceous shale and iron formation with locally intense quartz-sericite-magnetite alteration.

The Puck zone is the southernmost zone of mineralization on the Wolverine property, located ~6 km from the Wolverine deposit (Fig. 2). It differs slightly from the other zones in having abundant mafic rocks within the stratigraphy. The footwall stratigraphy consists of interlayered felsic volcaniclastic rocks and carbonaceous shales that are variably altered to quartz, sericite, and chlorite. Locally, the footwall contains ~347 Ma K-feldspar porphyritic intrusions like those in the Wolverine and Fisher zones (Piercey et al., 2008). Mineralization consists of sphalerite, chalcopyrite, and galena in stringer veins to massive sulfide in variably sericite altered, quartz- and feldspar-rich tuffaceous rocks. The immediate hanging wall consists of volcanic siltstone interlayered with carbonaceous shale that grades upward into magnetite iron formation and, locally, there are carbonate exhalative rocks (Peter et al., 2007). The upper hanging wall consists of gabbro intrusions and mafic dikes/sills interlayered with volcanic siltstone and carbonaceous shale, locally with peperitic textures.

Pb Isotope Geochemistry

Sampling and analytical methods

Samples of shales from the Wolverine deposit were collected from the Wolverine, Fisher, Sable, and Puck zones (Table 1). Sampling strategy was described in detail in Piercey et al. (2016), who also reported full chemical analyses for a wider set of samples, including those utilized for Pb isotope analyses in this paper. The Pb isotope data reported here (Table 1) were obtained from the leftover digests prepared for analyses of trace elements by inductively coupled plasma-mass spectrometry (ICP-MS). Agate mill-powdered 100-mg aliquots were digested with 2 ml of concentrated HF and 1 ml of concentrated HNO_3 (both subboiling distilled) in capped 30-ml Teflon beakers on a hot plate at 130°C for 72 h. After digestion, samples were evaporated to dryness, and the residues were converted twice with 1 ml of concentrated HNO_3 and then taken up in 10 ml of 20% v/v HNO_3. The solution was transferred to a 14-ml polystyrene test tube, centrifuged, and inspected for insoluble fluorides. If present, these were attacked with more HNO_3 until full dissolution. A gravimetric 2% liquid aliquot of this stock solution was removed for trace element analysis. The remainder of the solution was transferred back into the Teflon beaker and evaporated to dryness. When dry, the residue was converted to the bromide form by attacking twice with 1 ml of H_2O and one drop of concentrated HBr. Lead was purified from the converted stock solution using the HCl method of Kamber and Gladu (2009).

All solutions were analyzed using a Thermo X Series II quadrupole (Q)-ICP-MS. The trace elements, including Pb, Th, and U, were determined following the methodology explained in Kamber (2009) and Marx and Kamber (2010), yielding long-term U/Th and U/Pb reproducibility (n = 17) for reference material JA-2 of 2.098 ± 17 and 0.122 ± 1, respectively. Lead isotope ratios were obtained following the method described by Ulrich et al. (2010). Briefly, all purified Pb solutions were diluted to get a combined Pb signal of 2e6 cps to avoid tripping any individual signal into analogue detector mode. The very small mass bias during analysis was corrected for with interspersed analyses of NIST SRM 981 using the values published by Baker et al. (2004). Accuracy and external precision were monitored by analyzing interspersed NIST SRM 982 at the same concentration as the samples, yielding the following long-term (n = 200) average ratios: $^{207}Pb/^{206}Pb$ = 0.46696 ± 44, $^{208}Pb/^{206}Pb$ = 1.0005 ± 14, and $^{206}Pb/^{204}Pb$ = 36.744 ± 51. These are within the more precise multicollector data reported, for example, by Collerson et al. (2002).

Results

Lead isotope data are presented in Figure 4 in standard uranogenic and thorogenic plots with various growth curves, including the depleted mantle and old upper continental crust curves of Kramers and Tolstikhin (1997) and the shale curve of Godwin and Sinclair (1982). The shale curve is an empirical Pb isotope model approximating the Pb isotope compositions of sediment-hosted Pb-Zn occurrences found within the continental margin of western North America. It is interpreted to represent the crustal composition of the continental margin of the northern Cordillera and is also likely representative of the basement to the Yukon-Tanana terrane (e.g., Piercey and Colpron, 2009). The curve is an empirical model approximation and does not reflect the fact that the actual input data contain absolute variations in $^{207}Pb/^{204}Pb$ and $^{206}Pb/^{204}Pb$ around the curve. However, the main purpose of the curve is to provide a reference model to facilitate comparisons of regional Pb isotope datasets for other deposits (e.g., Mortensen et al., 2006). Variations in isotope composition between populations within our dataset are independent of the uncertainty of the curve, and we use it only as a reference for potential crustal Pb sources in the area.

Figure 4 shows separate panels for present-day Pb and initial Pb isotope compositions (corrected for U and Th decay

Table 1. Pb Isotope Data for Shales from the Wolverine Deposit

Sample no.	PK96-04, 254.7	PK96-04, 263.5	PK96-04, 264.5	PK96-04, 265.7	WV00-119, 78.9	WV00-119, 94.5
Drill hole	PK96-04	PK96-04	PK96-04	PK96-04	WV00-119	WV00-119
Depth (m)	254.7	263.5	264.5	265.7	78.9	94.5
Rock type	Argillite	Argillite	Argillite	Argillite	Argillite	Argillite
Stratigraphic position	Footwall	Footwall	Footwall	Footwall	HW (<10 m)	Footwall
Zone	Puck	Puck	Puck	Puck	Wolverine/ Lynx/Hump	Wolverine/ Lynx/Hump
Th (ppm)	4.49	5.37	5.71	5.29	2.05	4.80
U (ppm)	37.66	21.28	54.68	26.42	1.72	3.72
Pb (ppm)	12.40	13.65	21.21	16.46	8.06	13.59
$^{207}Pb/^{206}Pb$	0.6104	0.6515	0.6147	0.6586	0.8061	0.8101
1σ	0.0008	0.0009	0.0008	0.0009	0.0010	0.0011
$^{208}Pb/^{206}Pb$	1.486	1.595	1.493	1.611	1.987	2.004
1σ	0.001	0.001	0.001	0.001	0.000	0.001
$^{206}Pb/^{204}Pb$	26.271	24.433	26.077	24.163	19.460	19.418
1σ	0.039	0.036	0.038	0.036	0.019	0.029
$^{207}Pb/^{204}Pb$	16.036	15.918	16.029	15.914	15.687	15.731
1σ	0.024	0.023	0.024	0.023	0.015	0.023
$^{208}Pb/^{204}Pb$	39.030	38.982	38.926	38.936	38.668	38.906
1σ	0.058	0.057	0.057	0.057	0.037	0.057
$^{238}U/^{204}Pb$ (μ)	216	108	183	111	13.8	17.8
$^{232}Th/^{204}Pb$ (κ)	26.6	28.2	19.7	23.0	17.0	23.7

Sample no.	WV05-137, 98.5	WV05-144, 144.8	WV05-144, 167.5	WV05-144, 167.5	WV05-163, 130.6	WV05-163, 69.65
Drill hole	WV05-137	WV05-144	WV05-144	WV05-144	WV05-163	WV05-163
Depth (m)	98.5	144.8	167.5	167.5	130.6	69.65
Rock type	Argillite	Argillite	Argillite	Argillite	Argillite	Argillite
Stratigraphic position	HW (<10 m)	HW (>10 m, <Fe-fm)	HW (<10 m)	HW (<10 m)	HW (<10 m)	HW (>Fe-fm)
Zone	Wolverine/ Lynx/Hump	Wolverine/ Lynx/Hump	Wolverine/ Lynx/Hump	Wolverine/ Lynx/Hump	Wolverine/ Lynx/Hump	Wolverine/ Lynx/Hump
Th (ppm)	3.90	2.69	3.80	3.68	6.00	7.64
U (ppm)	51.03	2.69	27.58	26.63	2.52	1.93
Pb (ppm)	290.5	14.57	414.7	425.3	11.80	9.31
$^{207}Pb/^{206}Pb$	0.8200	0.8032	0.8300	0.8304	0.8095	0.8091
1σ	0.0011	0.0011	0.0010	0.0011	0.0010	0.0011
$^{208}Pb/^{206}Pb$	2.021	1.981	2.043	2.049	2.012	2.034
1σ	0.001	0.001	0.000	0.001	0.000	0.001
$^{206}Pb/^{204}Pb$	19.175	19.551	18.910	18.855	19.274	19.452
1σ	0.028	0.029	0.018	0.028	0.019	0.029
$^{207}Pb/^{204}Pb$	15.724	15.703	15.696	15.656	15.603	15.738
1σ	0.023	0.023	0.015	0.023	0.015	0.023
$^{208}Pb/^{204}Pb$	38.746	38.734	38.627	38.639	38.781	39.571
1σ	0.057	0.057	0.037	0.057	0.038	0.058
$^{238}U/^{204}Pb$ (μ)	11.3	11.9	4.12	4.16	13.8	13.6
$^{232}Th/^{204}Pb$ (κ)	0.90	12.3	0.59	0.59	33.9	55.5

Sample no.	WV05-174, 106.0	WV05-174, 183.1	WV05-174, 190.8	WV05-174, 192.5	WV95-02, 116.2	WV95-02, 98.5
Drill hole	WV05-174	WV05-174	WV05-174	WV05-174	WV95-02	WV95-02
Depth (m)	106	183.1	190.8	192.5	116.2	98.5
Rock type	Argillite	Argillite	Argillite	Argillite	Argillite	Argillite
Stratigraphic position	HW (<10 m)	HW (<10 m)	HW (<10 m)	HW (<10 m)	Footwall	Footwall
Zone	Wolverine/ Lynx/Hump	Wolverine/ Lynx/Hump	Wolverine/ Lynx/Hump	Wolverine/ Lynx/Hump	Sable	Sable
Th (ppm)	1.83	24.24	2.74	1.74	2.91	20.3
U (ppm)	0.43	7.01	2.11	1.24	1.32	4.40
Pb (ppm)	17.42	142.42	11.95	30.40	2,556.25	569.16
$^{207}Pb/^{206}Pb$	0.8332	0.8261	0.8067	0.8218	0.8336	0.8311
1σ	0.0011	0.0010	0.0010	0.0010	0.0011	0.0011
$^{208}Pb/^{206}Pb$	2.058	2.035	1.994	2.030	2.050	2.052
1σ	0.001	0.000	0.000	0.000	0.001	0.001
$^{206}Pb/^{204}Pb$	18.765	18.935	19.342	19.003	18.809	18.866
1σ	0.028	0.018	0.019	0.018	0.028	0.028
$^{207}Pb/^{204}Pb$	15.634	15.642	15.603	15.617	15.679	15.680
1σ	0.023	0.015	0.015	0.015	0.023	0.023
$^{208}Pb/^{204}Pb$	38.625	38.535	38.571	38.584	38.557	38.703
1σ	0.057	0.037	0.037	0.037	0.057	0.057
$^{238}U/^{204}Pb$ (μ)	1.59	3.15	11.4	2.61	0.033	0.496
$^{232}Th/^{204}Pb$ (κ)	6.93	11.3	15.3	3.80	0.075	2.36

Table 1. *(Cont.)*

Sample no.	WV95-20, 266.1	WV96-38, 257.5	WV96-38, 299.8	WV96-38, 303.8	WV96-38, 321	WV96-38, 361.8
Drill hole	WV95-20	WV96-38	WV96-38	WV96-38	WV96-38	WV96-38
Depth (m)	266.1	257.5	299.8	303.8	321	361.8
Rock type	Argillite	Argillite	Argillite	Argillite	Argillite	Argillite
Stratigraphic position	HW (<10 m)	HW (<10 m)	Footwall	Footwall	Footwall	Footwall
Zone	Wolverine/ Lynx/Hump	Fisher	Fisher	Fisher	Fisher	Fisher
Th (ppm)	3.01	2.02	2.63	8.92	4.87	1.98
U (ppm)	15.0	5.29	10.8	4.40	3.92	4.32
Pb (ppm)	109.0	3.91	9.84	12.8	13.1	13.1
$^{207}Pb/^{206}Pb$	0.8135	0.6545	0.7221	0.7672	0.7656	0.7763
1σ	0.0010	0.0009	0.0010	0.0010	0.0010	0.0010
$^{208}Pb/^{206}Pb$	2.001	1.604	1.782	1.912	1.900	1.907
1σ	0.000	0.001	0.001	0.000	0.001	0.000
$^{206}Pb/^{204}Pb$	19.257	24.270	21.918	20.518	20.567	20.229
1σ	0.019	0.036	0.032	0.020	0.030	0.020
$^{207}Pb/^{204}Pb$	15.667	15.886	15.827	15.740	15.747	15.703
1σ	0.015	0.023	0.023	0.015	0.023	0.015
$^{208}Pb/^{204}Pb$	38.537	38.940	39.052	39.225	39.068	38.571
1σ	0.037	0.057	0.058	0.038	0.058	0.037
$^{238}U/^{204}Pb$ (μ)	8.85	93.6	73.8	22.7	19.7	21.5
$^{232}Th/^{204}Pb$ (κ)	1.84	36.9	18.5	47.5	25.3	10.1

Sample no.	WV96-38, 379.5	WV96-38, 418.9	WV96-38, 452.1	WV96-38, 491.5	WV96-43, 338.4	WV96-43, 345.6
Drill hole	WV96-38	WV96-38	WV96-38	WV96-38	WV96-43	WV96-43
Depth (m)	379.5	418.9	452.1	491.5	338.4	345.6
Rock type	Argillite	Argillite	Argillite	Argillite	Argillite	Argillite
Stratigraphic position	Footwall	Footwall	Footwall	Footwall	HW (<10 m)	HW (<10 m)
Zone	Fisher	Fisher	Fisher	Fisher	Wolverine/ Lynx/Hump	Wolverine/ Lynx/Hump
Th (ppm)	5.03	11.6	8.40	4.84	4.54	1.72
U (ppm)	21.7	2.08	17.0	3.30	9.48	1.52
Pb (ppm)	18.5	2.16	38.4	9.98	48.9	30.2
$^{207}Pb/^{206}Pb$	0.6809	0.7688	0.7543	0.7815	0.8107	0.8188
1σ	0.0009	0.0010	0.0010	0.0011	0.0010	0.0010
$^{208}Pb/^{206}Pb$	1.668	2.060	1.876	1.954	1.996	2.018
1σ	0.000	0.001	0.001	0.001	0.000	0.000
$^{206}Pb/^{204}Pb$	23.298	20.464	20.855	20.053	19.355	19.092
1σ	0.023	0.030	0.031	0.030	0.019	0.018
$^{207}Pb/^{204}Pb$	15.864	15.733	15.732	15.671	15.692	15.632
1σ	0.015	0.023	0.023	0.023	0.015	0.015
$^{208}Pb/^{204}Pb$	38.863	42.153	39.134	39.175	38.632	38.524
1σ	0.038	0.062	0.058	0.058	0.037	0.037
$^{238}U/^{204}Pb$ (μ)	80.3	66.2	29.4	21.7	12.5	3.23
$^{232}Th/^{204}Pb$ (κ)	19.2	383	15.0	32.8	6.18	3.77

Sample no.	WV96-43, 404.2	WV96-43, 43.4	WV97-102, 126.95	WV97-102, 133.50	WV97-102, 72.10	WV97-102, 76.45
Drill hole	WV96-43	WV96-43	WV97-102	WV97-102	WV97-102	WV97-102
Depth (m)	404.2	43.4	126.95	133.5	72.1	76.45
Rock type	Argillite	Argillite	Argillite	Argillite	Argillite	Argillite
Stratigraphic position	Footwall	HW (>Fe-fm)	HW (>Fe-fm)	HW (>Fe-fm)	HW (>Fe-fm)	HW (>Fe-fm)
Zone	Wolverine/ Lynx/Hump	Wolverine/ Lynx/Hump	Wolverine/ Lynx/Hump	Wolverine/ Lynx/Hump	Wolverine/ Lynx/Hump	Wolverine/ Lynx/Hump
Th (ppm)	26.9	13.0	11.8	8.05	8.30	11.5
U (ppm)	10.1	3.49	2.80	3.06	2.07	2.74
Pb (ppm)	34.81	19.2	10.4	10.4	7.31	9.61
$^{207}Pb/^{206}Pb$	0.8007	0.8122	0.8075	0.8089	0.8058	0.8050
1σ	0.0010	0.0011	0.0011	0.0011	0.0011	0.0011
$^{208}Pb/^{206}Pb$	2.002	2.048	2.039	2.038	2.025	2.032
1σ	0.000	0.001	0.001	0.001	0.001	0.001
$^{206}Pb/^{204}Pb$	19.647	19.307	19.459	19.435	19.543	19.524
1σ	0.019	0.028	0.029	0.029	0.029	0.029
$^{207}Pb/^{204}Pb$	15.731	15.682	15.713	15.720	15.748	15.717
1σ	0.015	0.023	0.023	0.023	0.023	0.023
$^{208}Pb/^{204}Pb$	39.337	39.548	39.667	39.599	39.565	39.674
1σ	0.038	0.058	0.058	0.058	0.058	0.058
$^{238}U/^{204}Pb$ (μ)	18.9	11.9	17.6	19.3	18.6	18.7
$^{232}Th/^{204}Pb$ (κ)	52.2	45.8	77.1	52.6	76.9	81.0

Table 1. *(Cont.)*

Sample no.	WV97-105, 113.07	WV97-105, 143	WV97-105, 290	WV97-105, 343.5	WV97-105, 361.5	WV97-105, 57.8
Drill hole	WV97-105	WV97-105	WV97-105	WV97-105	WV97-105	WV97-105
Depth (m)	113.07	143	290	343.5	361.5	57.8
Rock type	Argillite	Argillite	Argillite	Argillite	Argillite	Argillite
Stratigraphic position	HW (>Fe-fm)	HW (>Fe-fm)	HW (>10 m, <Fe-fm)	HW (<10 m)	HW (<10 m)	HW (>Fe-fm)
Zone	Wolverine/ Lynx/Hump	Wolverine/ Lynx/Hump	Wolverine/ Lynx/Hump	Wolverine/ Lynx/Hump	Wolverine/ Lynx/Hump	Wolverine/ Lynx/Hump
Th (ppm)	11.1	7.90	8.11	2.97	4.12	13.4
U (ppm)	3.73	2.01	2.29	5.30	3.35	3.07
Pb (ppm)	12.1	9.27	2.89	87.7	28.0	6.99
$^{207}Pb/^{206}Pb$	0.8126	0.8086	0.7589	0.8283	0.8151	0.7962
1σ	0.0011	0.0011	0.0010	0.0011	0.0011	0.0010
$^{208}Pb/^{206}Pb$	2.044	2.037	1.940	2.045	2.015	2.025
1σ	0.001	0.001	0.000	0.001	0.001	0.000
^{206}Pb / ^{204}Pb	19.333	19.416	20.716	18.924	19.236	19.696
1σ	0.029	0.029	0.020	0.028	0.028	0.019
$^{207}Pb/^{204}Pb$	15.710	15.699	15.721	15.675	15.679	15.681
1σ	0.023	0.023	0.015	0.023	0.023	0.015
$^{208}Pb/^{204}Pb$	39.513	39.557	40.187	38.704	38.759	39.877
1σ	0.058	0.058	0.039	0.057	0.057	0.039
$^{238}U/^{204}Pb$ (μ)	20.1	14.2	53.3	3.88	7.70	29.0
$^{232}Th/^{204}Pb$ (κ)	61.9	57.6	195	2.25	9.79	131

Sample no.	WV97-105, 79.9	WV97-83, 181.3
Drill hole	WV97-105	WV97-83
Depth (m)	79.9	181.3
Rock type	Argillite	Argillite
Stratigraphic position	HW (>Fe-fm)	Footwall
Zone	Wolverine/ Lynx/Hump	Foot Claims
Th (ppm)	12.4	5.44
U (ppm)	3.51	21.6
Pb (ppm)	36.3	123.6
$^{207}Pb/^{206}Pb$	0.8228	0.8001
1σ	0.0011	0.0011
$^{208}Pb/^{206}Pb$	2.056	1.970
1σ	0.001	0.001
$^{206}Pb/^{204}Pb$	19.046	19.660
1σ	0.028	0.029
$^{207}Pb/^{204}Pb$	15.672	15.731
1σ	0.023	0.023
$^{208}Pb/^{204}Pb$	39.150	38.731
1σ	0.058	0.057
$^{238}U/^{204}Pb$ (μ)	6.26	11.4
$^{232}Th/^{204}Pb$ (κ)	22.9	2.95

Abbreviations: Fe-fm = iron formation, HW = hanging wall

to 350 Ma, the approximate age of mineralization in the Wolverine deposit—e.g., Piercey et al., 2008). All data are listed in Table 1.

In the present-day $^{207}Pb/^{204}Pb$-$^{206}Pb/^{204}Pb$ diagram (Fig. 4A), two distinctive populations of samples are readily identified. The first population has a limited range of relatively unradiogenic $^{206}Pb/^{204}Pb$ (<20) but shows considerable variability in $^{207}Pb/^{204}Pb$ (Fig. 4A), generally much higher than depleted mantle. These samples plot in the vicinity of present-day old upper continental crust and shale, and significantly above a hypothetical 350 Ma reference isochron starting from a contemporaneous mantle composition. The samples define a positively sloping array with a slope much steeper than a 350 Ma isochron. The tie line between present-day depleted mantle and present-day upper continental crust plots through the array. A subset of samples within this population from the immediate Wolverine hanging wall has lower $^{207}Pb/^{204}Pb$ values at a given $^{206}Pb/^{204}Pb$ (Fig. 4B), whereas samples from the uppermost hanging wall tend to higher $^{207}Pb/^{204}Pb$ at a given $^{206}Pb/^{204}Pb$; other samples from the Sable zone and Wolverine footwall tend toward the center of this array and cluster proximal to the shale curve (Fig. 4A). Overall, this distribution of Pb isotope ratios is similar to those found in sulfide minerals within the Wolverine deposit and in massive sulfides throughout the Finlayson Lake district (Mortensen et al., 2006; Layton-Matthews et al., 2013).

A second, more striking population of samples exists in $^{207}Pb/^{204}Pb$-$^{206}Pb/^{204}Pb$ isotope space, characterized by high $^{206}Pb/^{204}Pb$ (>20), with Puck zone samples having the highest $^{206}Pb/^{204}Pb$ values (24.2–26.3; Fig. 4A, C). The group encompasses samples from the Fisher, Sable and, to a lesser extent, Wolverine hanging wall. The samples plot along a linear array with a slope similar to that of the hypothetical 350 Ma isochron, albeit transposed to significantly higher $^{206}Pb/^{204}Pb$.

The slope of this array suggests that the high $^{206}Pb/^{204}Pb$ population underwent a U enrichment event that was coincident with deposit formation (see "Discussion" and "Summary").

An attempt was made to calculate initial Pb isotope compositions to test whether better constraints on the sources of Pb were possible, although it is well established that the correction for U decay assumes closed-system behavior for the two potentially mobile elements U and Pb. Initial isotope ratios are shown in Figure 4C. The age correction significantly reduces the spread in $^{207}Pb/^{204}Pb$ and $^{206}Pb/^{204}Pb$ ratios. Figure 4C shows a tie line between 350-m.y.-old mantle and old upper continental crust, which has a composition nearly identical to the local northern margin of the Cordillera (i.e., the shale curve). The samples show significant scatter, likely the result of true variability in initial Pb isotope composition, as well as error introduced by correction for U decay (e.g., DeWolf and Mezger, 1994). The initial ratios plotting to the left of the 350 Ma tie line almost certainly represent overcorrection for U decay resulting from subrecent Pb loss from the shale. Regardless, the samples with the highest $^{207}Pb/^{204}Pb$ ratios represent Pb from a source with a high time-integrated U/Pb ratio, whereas those with lower $^{207}Pb/^{204}Pb$ ratios have

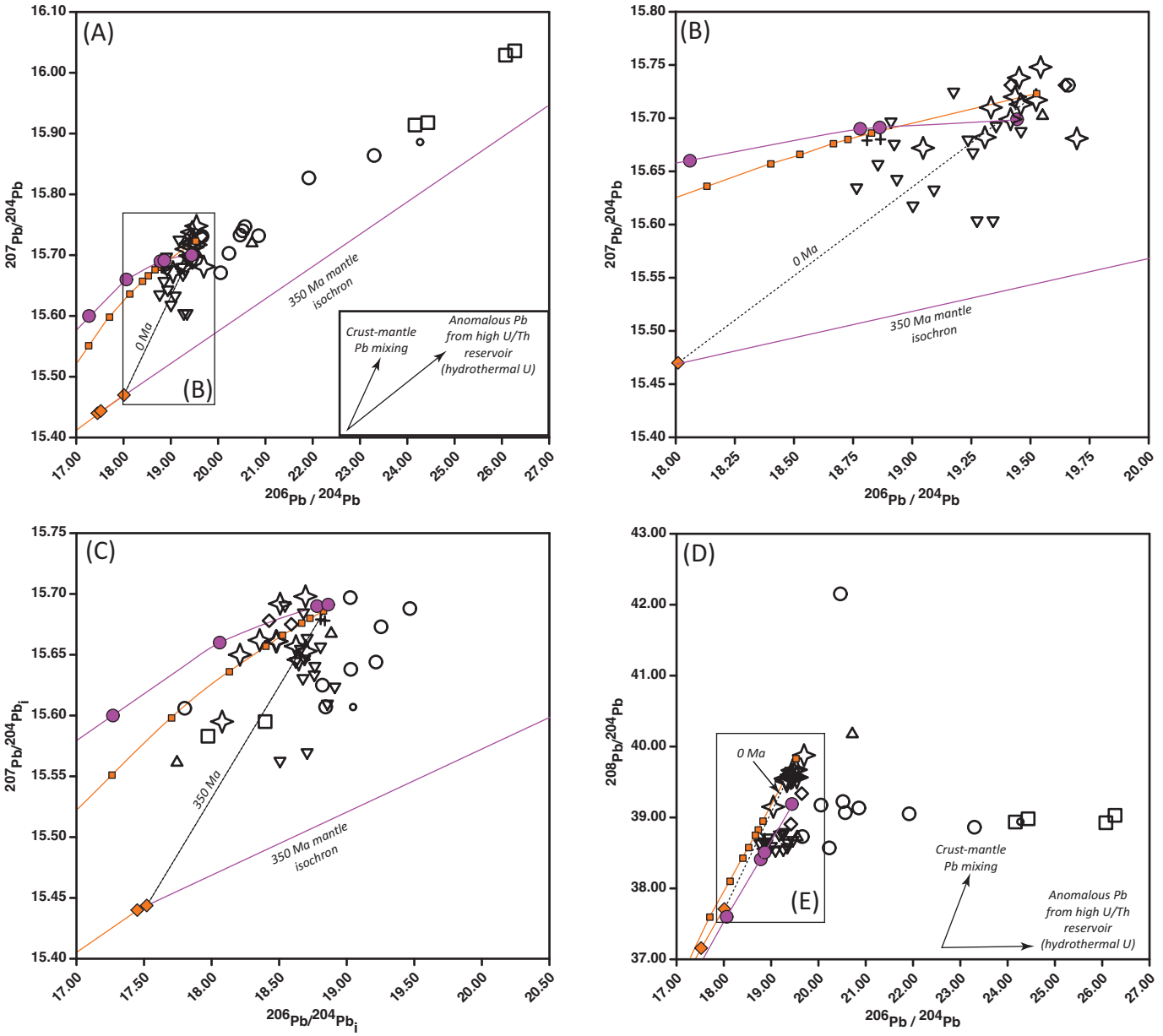

Fig. 4. Pb isotope data for shales from the Wolverine deposit. A) $^{207}Pb/^{204}Pb$-$^{206}Pb/^{204}Pb$. B) Close-up of data array in (A). C) Age-corrected $^{207}Pb/^{204}Pb$-$^{206}Pb/^{204}Pb$ plot with 350 Ma tie line. D) $^{208}Pb/^{204}Pb$-$^{206}Pb/^{204}Pb$. E) Close-up of data array in (D). F) Age-corrected $^{208}Pb/^{204}Pb$-$^{206}Pb/^{204}Pb$ plot with 350 Ma tie line. Shown in all diagrams are the curves for the depleted mid-ocean ridge basalt mantle (DMM) and old upper continental crust (UCC) from Kramers and Tolstikhin (1997), and the shale curve, a local Pb isotope growth curve for the Cordilleran margin, from Godwin and Sinclair (1982). The 350 Ma depleted mantle reference isochron was calculated from DMM values at 350 Ma and with subsequent decay toward present day. Abbreviations: Fe-fm = iron formation, FW = footwall, HW = hanging wall.

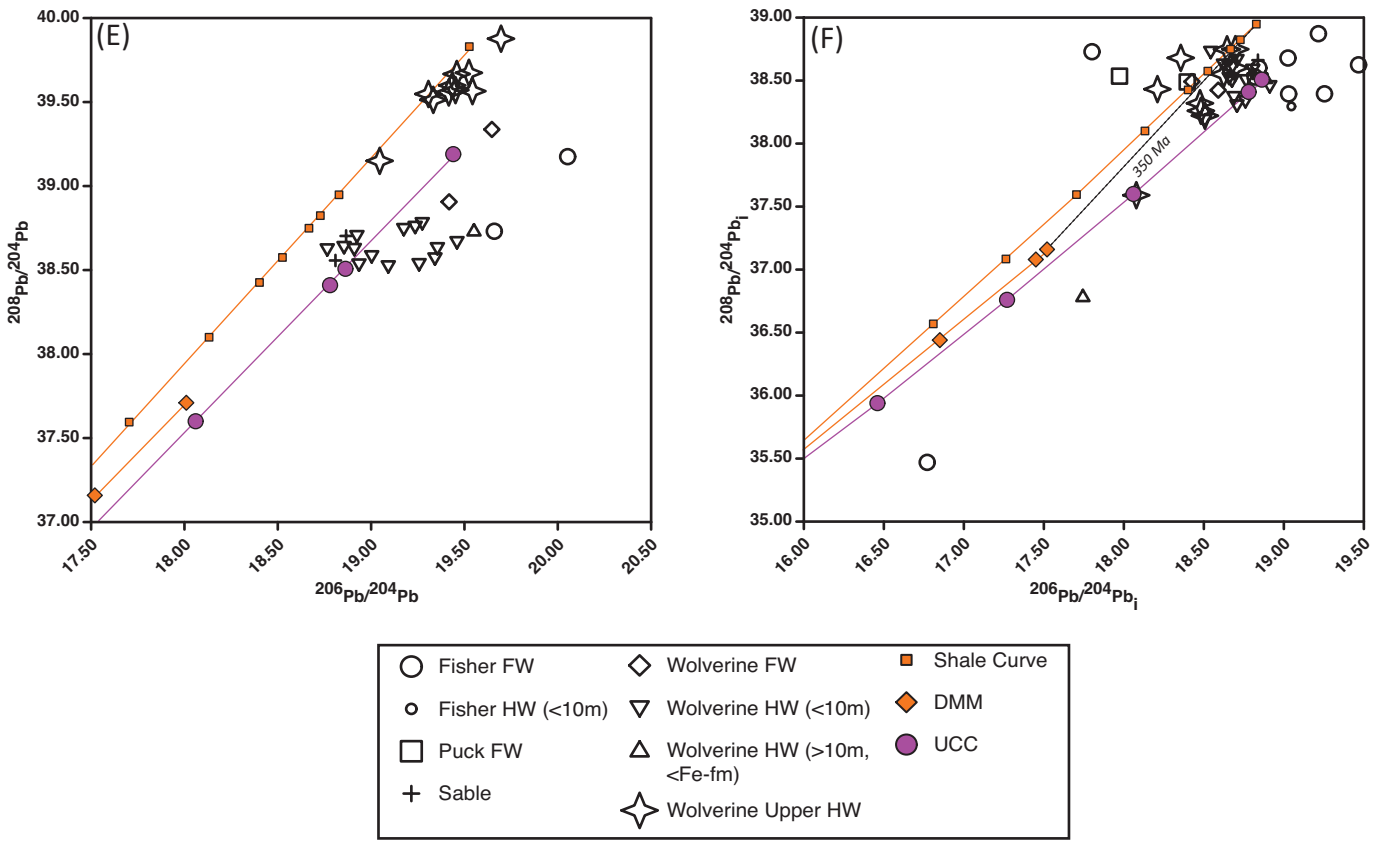

Fig. 4. *(Cont.)*

a more significant juvenile component. None of the samples contain true juvenile depleted mantle-derived Pb.

In present-day $^{208}Pb/^{204}Pb$-$^{206}Pb/^{204}Pb$ space (Fig. 4D), a similar clustering into two distinctive groups exists. In this diagram, the high $^{206}Pb/^{204}Pb$ samples show a conspicuous horizontal array with very restricted $^{208}Pb/^{204}Pb$ (38.57–39.23). Globally speaking, this type of behavior is rare (e.g., Zartman and Doe, 1981), particularly in silicate rocks, as it implies strong ingrowth of ^{206}Pb and limited to inexistent ingrowth of ^{208}Pb. This is a reflection of unusually high U/Th ratios of the rocks, resulting in characteristically low $^{208}Pb/^{206}Pb$ ratios (see Table 1; ratios of 1.5–2.0 instead of the canonical terrestrial ratio of 2.2). The second group of samples, which in the uranogenic diagram showed spread in $^{207}Pb/^{204}Pb$ but quite limited $^{206}Pb/^{204}Pb$ variability (Fig. 4A), also has considerable variability in $^{208}Pb/^{204}Pb$ (Fig. 4E). It is worth noting that the local shale curve deviates significantly from the global upper continental crust curve in $^{208}Pb/^{204}Pb$ evolution. It can be seen that samples from the uppermost hanging wall of the Wolverine zone have very high $^{208}Pb/^{204}Pb$ at a given $^{206}Pb/^{204}Pb$, clustering proximal to the shale curve (Fig. 4E). With rare exceptions, all other samples from the Fisher, Puck, and Wolverine zones plot proximal to the global, old upper continental crust and to the right of a tie line between modern depleted mantle and local shale (Fig. 4E). The Sable zone samples range between both arrays. Age-corrected $^{208}Pb/^{204}Pb$ -$^{206}Pb/^{204}Pb$ data show a similar array with most samples clustering between the mantle and shale curves, but U overcorrection (Fig. 4F) distorts the data to the point where present-day systematics are more informative.

The combined isotopic variability in $^{208}Pb/^{204}Pb$ -$^{206}Pb/^{204}Pb$-$^{206}Pb/^{204}Pb$ space of the less radiogenic group of shales shows that Pb in the district was sourced from distinctive continental sources.

Discussion

Lead isotope systematics on their own suggest that the studied shales can readily be grouped into two populations: one with a present-day Pb isotope composition dominated by U but not Th decay since 350 Ma and a second with a Pb isotope ratio variation mainly inherited from the source, ranging from highly crustal in character to more juvenile. Here, the information from Pb isotope systematics is combined with high-precision trace element data for the same rocks (originally published and discussed in the context of a larger suite by Piercey et al., 2016). The combined data reveal the existence of three populations of shales, with distinctive time-integrated Th-U-Pb histories, which have potential significance for base metal exploration in shale-rich base metal-bearing basins.

The high-U/Th, high-U/Pb population

This group of samples stands out both in uranogenic and thorogenic Pb isotope space because of its elevated present-day $^{206}Pb/^{204}Pb$ but low $^{208}Pb/^{204}Pb$ ratios (Fig. 4A, D). The samples define a reasonably tight array in common Pb isotope space with a slope compatible with the known age of mineralization. Insight into the cause of the strong ^{206}Pb excess can be derived from the orientation of the data array in $^{208}Pb/^{204}Pb$-$^{206}Pb/^{204}Pb$ space (Fig. 4D). Given that ^{208}Pb is derived from

the decay of ^{232}Th, the horizontal array suggests that the source must have been unusually enriched in U but depleted in Th, resulting in a very low time-integrated Th/U ratio. Indeed, the samples with elevated $^{206}Pb/^{204}Pb$ ratios coincide with very high U enrichment (U_{EF}) values (see Algeo and Tribovillard, 2009) and very low (<0.5) Th/U ratios (Fig. 5A, B), consistent with strong preferential U enrichment. However, it is also notable that in $^{206}Pb/^{204}Pb$-U_{EF} and Th/U space, there is a second group of samples that shows variable but generally low Th/U (ranging from typical crustal values of 4 to <0.5) that does not have elevated $^{206}Pb/^{204}Pb$. On their own, Pb isotopes would have failed to recognize this population, which will be discussed after the origin of the U enrichment is explored here for the first group.

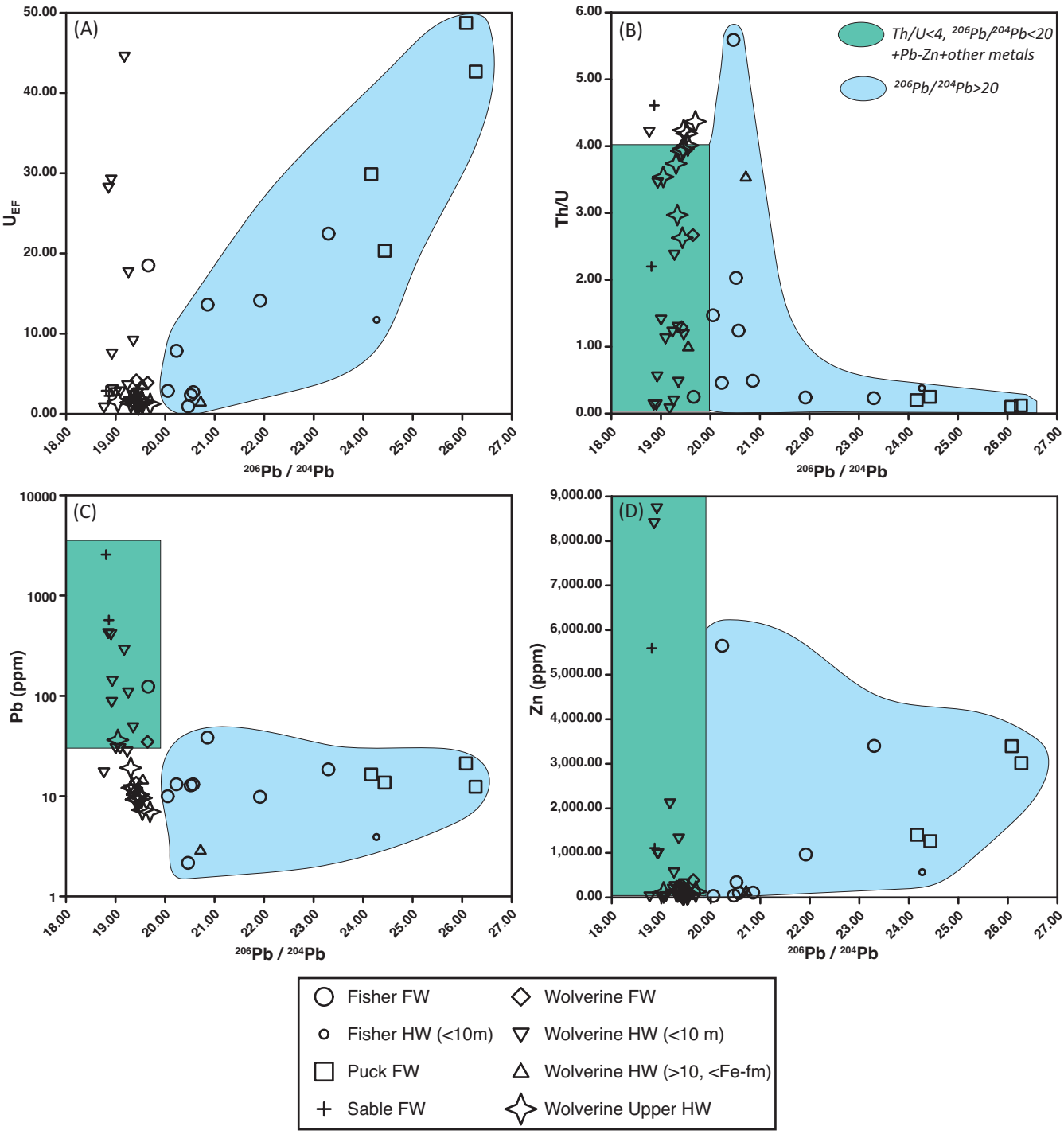

Fig. 5. $^{206}Pb/^{204}Pb$ versus various trace element ratios and concentrations: (A) U enrichment (U_{EF}) where $U_{EF} = (U_{sample}/Al_{sample})/(U_{PAAS}/Al/_{PAAS})$ (PAAS = Post-Archean Australian Shale; from Algeo and Tribovillard, 2009), (B) Th/U, (C) Pb, and (D) Zn. Abbreviations: Fe-fm = iron formation, FW = footwall, HW = hanging wall.

The most likely source for excess U is seawater, which has constituted a significant geochemical reservoir for this element (but not Th) since oxygenation of the atmosphere (e.g., Collerson and Kamber, 1999; Henderson, 2002). Because oxygenated seawater has several other characteristic features, it is possible to test whether U enrichment was indeed driven by seawater-derived fluids. Figure 6 shows that samples with high $^{206}Pb/^{204}Pb$ have strongly superchondritic Y/Ho ratios, reaching values as high as 40 to 50, which is a hallmark feature of saline waters like seawater (e.g., Nozaki et al., 1997) and minerals precipitated from such fluids (e.g., Kamber et al., 2015). Furthermore, the samples with radiogenic Pb also exhibit additional diagnostic geochemical features found in seawater: superchondritic Zr/Hf ratios (Fig. 6B; Bau, 1996),

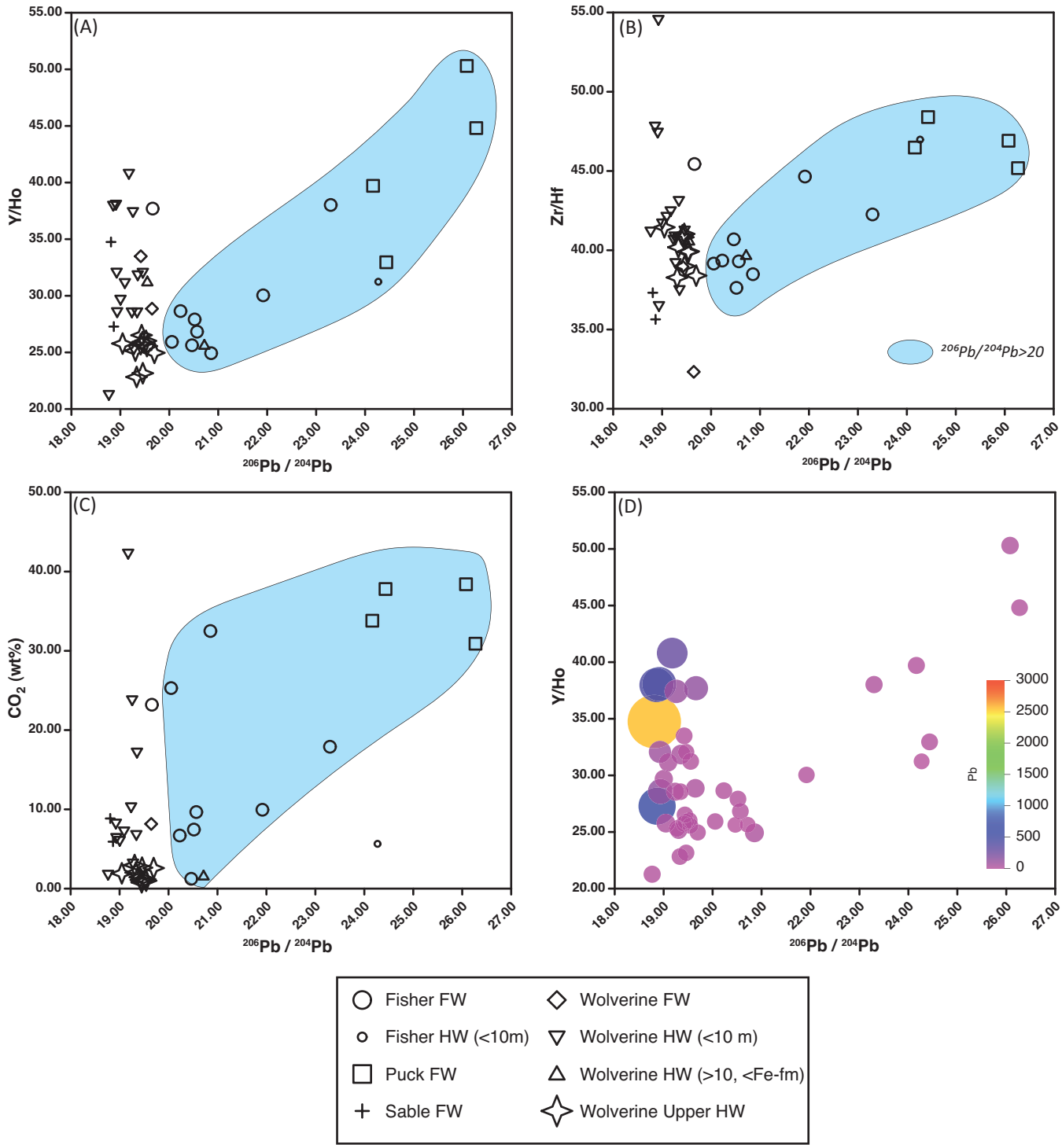

Fig. 6. $^{206}Pb/^{204}Pb$ versus various proxies for seawater input: (A) Y/Ho, (B) Zr/Hf, (C) CO_2, and (D) Y/Ho. In panel D, symbol size is proportional to Pb content of the samples. Abbreviations: Fe-fm = iron formation, FW = footwall, HW = hanging wall.

elevated Mo_{EF} (App. 1; Algeo and Tribovillard, 2009), and negative Ce anomalies (Ce/Ce*, App. 2; e.g., Bau and Dulski, 1999). Elevated Y/Ho and Zr/Hf are both products of elemental distribution that was not charge and radius controlled (CHARAC; Bau, 1996). Yttrium and Ho and Zr and Hf are geochemical twins and rarely fractionate from one another in nature; however, seawater and materials that have inherited a seawater signature generally have non-CHARAC behavior and elevated Y/Ho and Zr/Hf values (Bau, 1996; Firdaus et al., 2011). On its own, elevated Zr/Hf in sedimentary rocks like shales could potentially reflect the "zircon effect" (e.g., Linnen and Keppler, 2002). However, the inverse relationship between Zr/Hf and Ce/Ce* (App. 2), which is elevated in zircon (e.g., Ballard et al., 2002) but <1.0 in oxygenated seawater (e.g., Kamber et al., 2015), argues against the zircon effect being responsible for the elevated Zr/Hf signatures in the Wolverine shales.

In terms of the likely mineralogical host of the elements deposited into the shale from seawater, it is worth noting that the high $^{206}Pb/^{204}Pb$ samples are rich in CO_2 (Fig. 7), consistent with the speciation of U as uranyl carbonate ions (e.g., $UO_2(CO_3)_3^{4-}$; Davies et al., 1964; Dahlkamp, 1993; Macfarlane and Miller, 2007). It is therefore likely that the excess U is hosted in carbonate that precipitated from fluids that originated as oxygenated seawater. Supporting observations for this hypothesis from the greater Wolverine deposit area include abundant carbonate alteration throughout the Wolverine deposit and surrounding area (Bradshaw et al., 2008); the presence of carbonate-rich exhalites in the Wolverine deposit in the immediate hanging wall to mineralization and along strike (Peter et al., 2007); and shales from the Wolverine Basin with high CO_2 and carbonate alteration and high Y/Ho (Piercey et al., 2016). Piercey et al. (2016) argued that the elevated Y/Ho and CO_2 enrichment was due to late-stage hydrothermal overprinting by low-temperature hydrothermal fluids and, given the correlation between Y/Ho, CO_2, Th/U, U, and U_{EF} (figs. 7, 9b in Piercey et al., 2016), we extend this argument to fluids also having transported U as $UO_2(CO_2)_3^{4-}$ and deposited U in carbonate-rich shales.

While the origin of CO_2 and U is very likely from seawater, the exact mechanism of seawater overprinting in the Wolverine VMS system has not been sufficiently elucidated. The presence of the carbonate exhalative rocks with low-temperature hydrothermal signatures (Peter, 2003) in the hanging wall of the deposit and carbonate alteration in both the footwall and into the hanging wall of the deposit (Bradshaw et al., 2008) suggests that the carbonate alteration was both synchronous with and postdated sulfide deposition. In modern seafloor systems, it is common for seawater to be entrained in the near-vent environment (up to depths of 50 m below the seafloor) during black smoker activity (Tivey et al., 1995; Hannington et al., 1998; Humphris and Tivey, 2000; Tivey, 2007) with seafloor-altered basalt showing elevated U/Th ratios (e.g., Staudigel et al., 1996). At oceanic spreading centers, much deeper seawater penetration into the mantle portion of the plate is also inferred from the metasomatism of serpentinite (e.g., Kodolányi et al., 2011), causing highly radiogenic $^{206}Pb/^{204}Pb$ but low $^{208}Pb/^{204}Pb$ ratios, similar to those observed in this study (Pettke et al., 2018). We envisage a related process of shallow and deep fluid circulation at the Wolverine deposit. In the back-arc setting, deep circulation of hydrothermal fluids leached Pb from the basement (and other metals; see "The high-U/Th, low-U/Pb population," below), whereupon venting resulted in near-vent entrainment of oxygenated seawater rich in $UO_2(CO_2)_3^{4-}$ close to the surface (Fig. 8). Near-surface seawater infiltration of the hydrothermal system resulted in

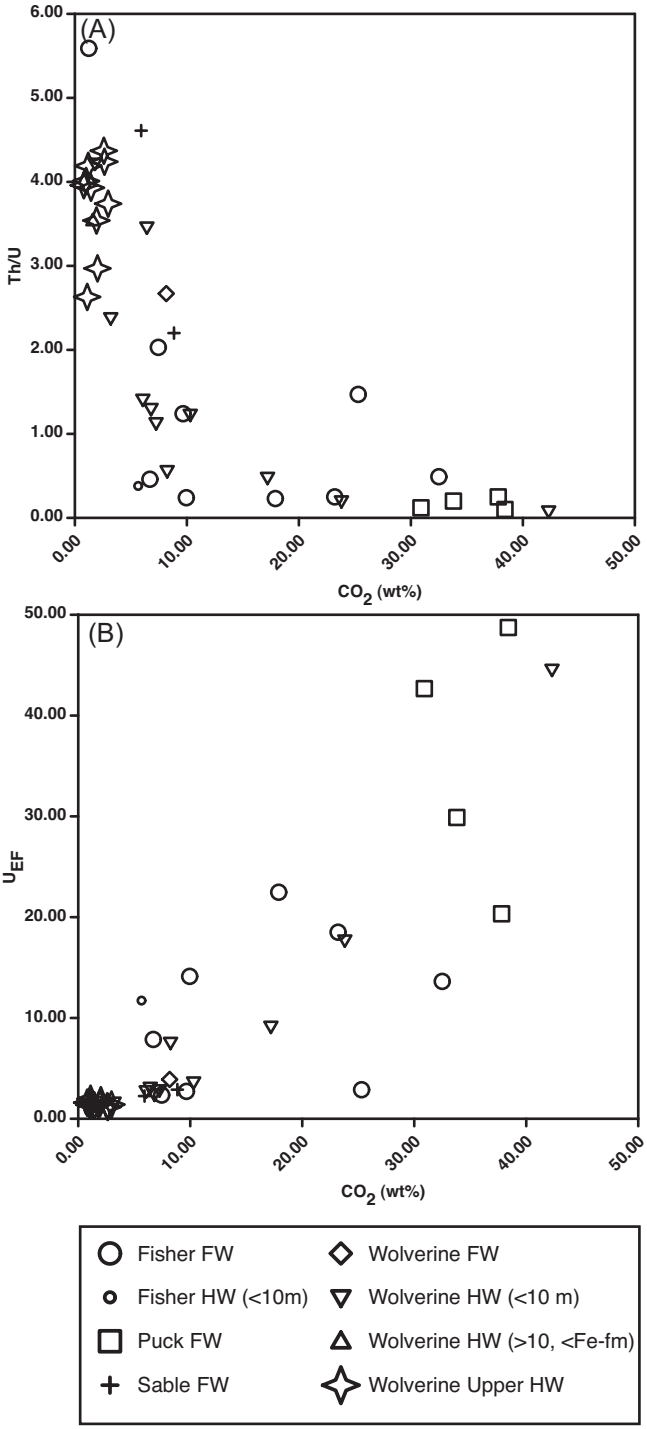

Fig. 7. CO_2 (proxy for carbonate alteration) versus (A) Th/U and (B) U enrichment (U_{EF}), illustrating the strong control that carbonate alteration has on the U distribution in the Wolverine shales. Abbreviations: Fe-fm = iron formation, FW = footwall, HW = hanging wall.

carbonate alteration and U enrichment of footwall rocks and shales intimately intercalated with mineralization as well as those slightly distal from mineralization (10s of meters; Fig. 8). Furthermore, this seawater ingress into the hydrothermal environment continued post-sulfide deposition, further enriching the near-vent shales in U. Over time, those shales with U>>Pb would evolve to high $^{206}Pb/^{204}Pb$ compositions due to ^{238}U decay, as observed in the high-U/Th and -U/Pb population (Figs. 4, 8).

The high-U/Th, low-U/Pb population

We noted earlier that, in $^{206}Pb/^{204}Pb$-U_{EF} and Th/U space (Fig. 5A, B), there is also a sample population with variable but generally very low Th/U and high U_{EF} that does not have elevated $^{206}Pb/^{204}Pb$. This group also has elevated Y/Ho, Zr/Hf, CO_2, and Mo_{EF} and low Ce/Ce* (Fig. 6; Apps. 1, 2) and therefore underwent carbonate alteration. However, within this population the U enrichment failed to measurably impact the present-day Pb isotope composition, and the data form a vertical trend and exhibit a lower, near-constant $^{206}Pb/^{204}Pb$ despite elevated CO_2, Y/Ho, Zr/Hf, and U (Figs. 4, 5). The reason for this difference is that these samples also have anomalous Pb, with concentrations as high as 2,500 ppm (Fig. 5C). The effect of Pb content on Pb isotope composition and carbonate fluid alteration is illustrated in Figure 6D, where the symbol size is proportional to Pb content, showing that only those samples with low Pb content and high Y/Ho ratio show a radiogenic $^{206}Pb/^{204}Pb$ ratio.

The origin of the Pb enrichment can be elucidated by extending the analysis to further base metals. Notably, the samples enriched in Pb also have high concentrations of Zn (Fig. 5D), as well as Tl, Pb, Sn, and W and, to a lesser extent, Cu and Mo_{EF} (App. 1). These metal enrichments in shale are inherited from the original mineralization associated with the Wolverine deposit and, because of the Pb-rich nature of mineralization, their Pb isotope composition was essentially buffered. Namely, they contained sufficient original Pb from mineralization such that any radiogenic ^{206}Pb from ^{238}U decay was too insignificant to change the $^{206}Pb/^{204}Pb$ ratios appreciably (e.g., Figs. 5C-D, 8). Only the combined evidence from Pb isotopes and trace element systematics can be used to reconstruct the two-stage process of base metal mineralization and carbonate alteration in these samples.

The crustal U/Th and U/Pb population

The final population of shales has crustal Y/Ho of approximately 24 to 28 (e.g., Kamber et al., 2015) and relatively low present-day $^{206}Pb/^{204}Pb$ (Fig. 6A). They have crustal to somewhat elevated Zr/Hf (Fig. 6B) between 35 and 40 (e.g., David et al., 2000) and lack elevated carbonate content (Fig. 6C). In common Pb isotope space, they broadly plot in the position of the local shale evolution curve (i.e., shale curve of Godwin and Sinclair, 1982), which is very similar to the global old upper crust evolution curve (Fig. 4). The majority of these samples are from the upper hanging wall and footwall of the Wolverine deposit (Fig. 4B). In thorogenic Pb isotope space (Fig. 4E), it is evident that only the Wolverine upper hanging-wall samples plot close to the local shale curve, whereas Wolverine footwall samples plot closer to the global upper continental crust evolution line. In summary, the Pb isotope composition of the Wolverine upper hanging-wall samples simply represents local detritus, unaffected by base metal-mineralizing fluids and not overprinted by carbonate alteration.

An important finding of this study is the clear distinction in Pb isotope composition between local shale (represented by Wolverine upper hanging wall) and the mildly base metal mineralized samples of the immediate hanging wall. At a given $^{206}Pb/^{204}Pb$, the immediate hanging-wall samples have both significantly lower $^{207}Pb/^{204}Pb$ and $^{208}Pb/^{204}Pb$ ratios than local shale (Fig. 4B, E). This could mean that the original detritus had a different crustal origin (and a different Pb isotope composition) and/or that the original detrital Pb was overwhelmed by extraneous Pb deposited from the mineralizing fluid. In uranogenic space, the Wolverine samples define a broad mixing array from local evolved crust toward more juvenile (mafic?) sources (depleted mantle). This general trend is compatible with the stratigraphy of the deposit. For example, mafic rocks from the deposit in the Puck zone and regionally have juvenile isotopic signatures (Piercey et al., 2006) and could have produced detritus with mantle-like Pb isotope signatures. Similarly, felsic and sedimentary rocks from the deposit and regionally have very evolved Pb-Nd-Sr-Hf isotope signatures, and most have abundant detrital and inherited zircons with Paleoproterozoic and Archean ages (i.e., old continental crust; Mortensen, 1992; Creaser et al., 1997; Murphy et al., 2006; Piercey et al., 2008; Piercey and Colpron, 2009). Therefore, mixing both of local rocks from within the Wolverine Basin and regionally from elsewhere in the Finlayson Lake district can be explained by the broader Pb isotope mixing array in uranogenic Pb space (Figs. 4A-C, 8).

Piercey et al. (2008, 2017) noted that there was evidence for juvenile input into footwall porphyritic rhyolites to the deposit and argued that this reflected injection of basalt beneath the Wolverine back-arc basin. Thus, it is possible that the more juvenile Pb isotope signatures present in the immediate hanging wall to the Wolverine deposit and Sable zone shales may reflect (1) deeply penetrating fluids that leached deeper juvenile basaltic basement, (2) the coincidence of mafic eruptions and juvenile detritus deposited in the shales, and/or (3) juvenile magmatic fluids/volatile Pb contributions from magmatic products at depth (Fig. 8).

When the $^{208}Pb/^{204}Pb$ ratios of the Wolverine hanging-wall samples are plotted against the inverse Pb isotope composition (App. 3), it is evident that even those immediate hanging-wall shales that have seen the least Pb enrichment (i.e., with the highest 1/Pb) have substantially lower $^{208}Pb/^{204}Pb$ than shales from the upper hanging wall (i.e., local shale). This argues in favor of a different provenance of the immediate hanging-wall shale, which has a more juvenile component. The thorogenic Pb isotopes shed further light onto the origin of this more juvenile Pb, which plots to the right of a mixing line between local shale and depleted mantle both in present-day (Fig. 4E) and initial Pb (Fig. 4F). In terms of Th/U systematics, the Pb in the mildly mineralized immediate hanging wall of the Wolverine samples thus likely had three sources: local shale, juvenile mantle, and a second crustal source resembling global old upper continental crust (e.g., Fig. 8). Similar Pb isotope compositions have been reported from ores from the stratigraphically lower Fyre Lake Formation in the Finlayson district by Mortensen et al. (2006). Thus, the base metal

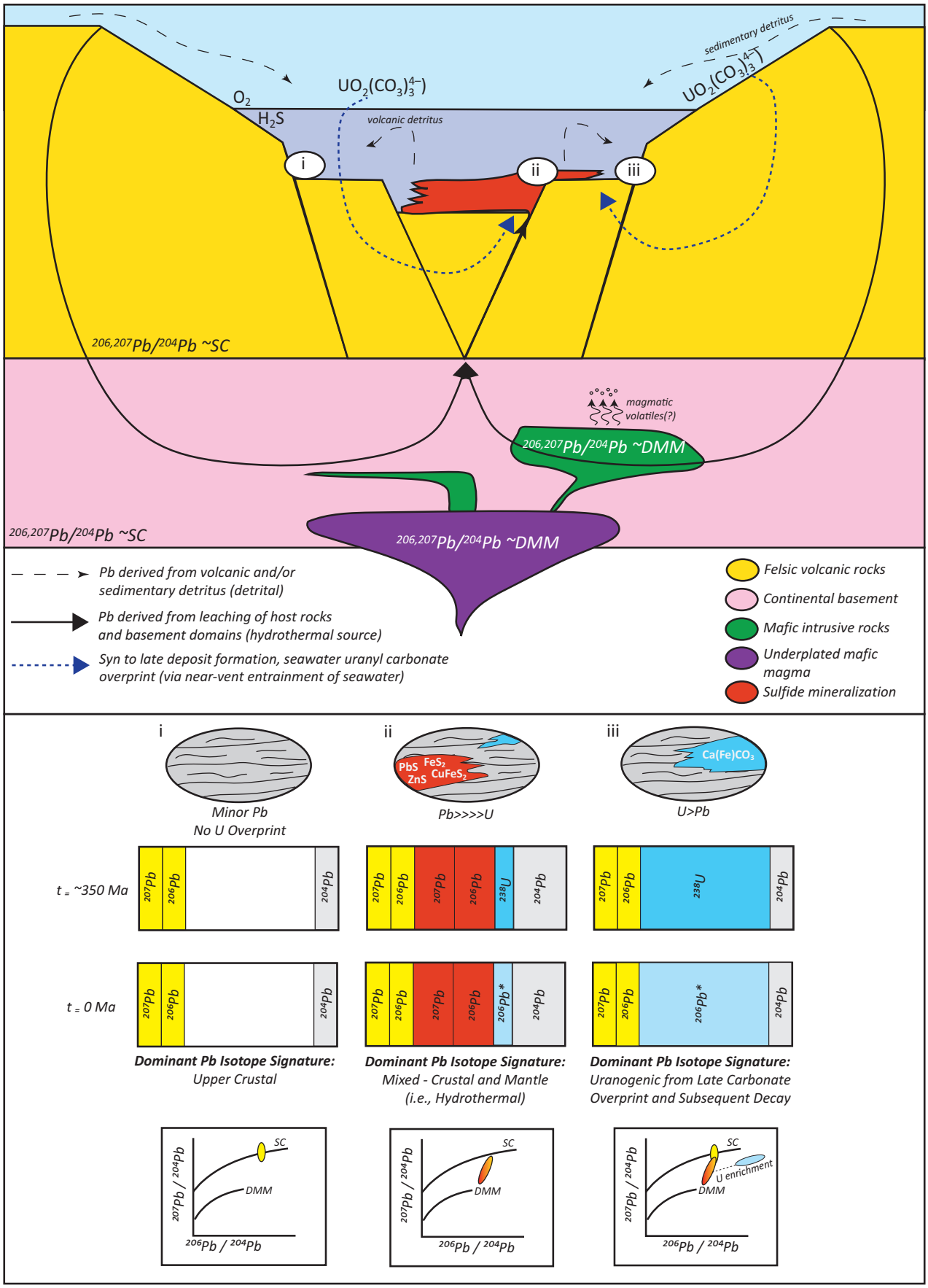

mineralization happened at a time when there was potentially juvenile and evolved detrital input, deep crustal fluid circulation and potential leaching of both felsic and mafic source rocks, and/or Pb derived from mafic (± felsic) magma devolatilization (Fig. 8).

Although the samples from the population with radiogenic present-day $^{206}Pb/^{204}Pb$ cannot accurately be back-corrected for U decay, the position of their linear arrays nonetheless permits a broad assessment of the origin of Pb in the carbonate-rich fluids. Both in uranogenic and thorogenic space (Fig. 4A, D), the linear arrays project more closely to the position of the immediate rather than upper hanging wall of the Wolverine deposit (cf. Fig. 8, panel iii). Thus, the carbonate-bearing fluids that percolated in shales of the Fisher and Puck zone footwall sequences either did not deposit any extraneous Pb into originally quite juvenile Pb of the shales (i.e., the juvenile signature was already in the shale) or scavenged juvenile Pb during circulation and leaching of deeper basement/footwall rocks.

Summary

The Pb isotope systematics of the studied shales can be summarized in terms of time-integrated Th/U/Pb evolution, illustrated schematically in Figure 8. The most distal (barren) shales recorded neither extraneous Pb nor U addition. Their Pb isotope composition at 350 Ma records information about the source of detritus, where there was mixing between felsic and more juvenile igneous detritus as well as sediment from evolved, upper crustal-like sources. Even in barren, distal section parts of the mineralized system at Wolverine, however, there are variations in shale Pb isotope composition that have the potential to aid exploration because the episodes of input of juvenile material are readily recorded in Pb due to the substantial differences in continental vs. mantle Pb. Due to their typically crustal U/Pb and Th/U ratios, distal shales evolve along the generic crustal Pb isotope model trajectories to the present day, without noteworthy deviations in the $^{207}Pb/^{206}Pb$ ratio (Figs. 4, 8).

Moving more proximal to mineralization (i.e., 10s to 100s of meters), there are weakly mineralized shales with the predominant feature of carbonate alteration from fluids that originated as seawater, likely from ingress of seawater into the Wolverine hydrothermal system in the near-vent environment (within 50 m of the seafloor). These fluids precipitated carbonate, U (as $UO_2(CO_2)_3^{4-}$), and other seawater-diagnostic elements (Mo, rare earth elements) into the shale (Fig. 8), without, however, significantly affecting the Pb budget at the time of alteration, probably because Pb has a very low residence time and concentration in seawater (e.g., von Blanckenburg et al., 1996). Even within the relatively modest time span of 350 m.y., the strong U enrichment proximal to the hydrothermal vents resulted in significant $^{206}Pb/^{204}Pb$ anomalies in the CO_2-U–rich shales.

In near-vent environments and mineralized zones (i.e., close to massive sulfide mineralization), the same type of seawater-derived CO_2-U alteration occurred, superimposing characteristic marine trace element signatures (high U/Th, Zr/Hf, Y/Ho, and negative Ce anomalies) on the shales. However, due to earlier (or synchronous) mineralization with Pb, Zn, Sn, Tl, and other base metals, the addition of significant seawater-derived U did not appreciably change the shale Pb isotope composition over time because the Pb in the shale is buffered by the Pb from mineralization (i.e., has juvenile Pb isotope signatures; Fig. 8).

The results presented herein illustrate how whole-rock Pb isotopes combined with trace element geochemistry have great potential for discriminating near-vent and mineralized zones in shale-rich hydrothermal environments. In particular, near-vent environments in the Wolverine deposit can be identified by anomalous $^{206}Pb/^{204}Pb$ ratios coupled with high Y/Ho, Zr/Hf, CO_2, and U contents, whereas immediate proximity to mineralization exhibits more restricted Pb isotope compositions, often lower, but also containing high Y/Ho, Zr/Hf, CO_2, and U contents, but with anomalous base and trace metals (Figs. 6–8; App. 1). Barren samples with little or no mineralization have typical crustal compositions but no evidence

Fig. 8. Model explaining the hydrothermal evolution of the Wolverine VMS deposit and the potential origins of Pb in its various shales. The deposit setting was a locally restricted anoxic basin that formed during ~350 Ma back-arc extension along the western edge of North America within the Yukon-Tanana terrane (Piercey et al., 2016). The potential Pb sources included detrital Pb, deeply sourced Pb from basement transported by fluids, and largely radiogenic (uranogenic Pb) that has formed from the decay of U, advected by shallow hydrothermal fluids derived from seawater.

The detritus had sedimentary and volcanic origins, and its Pb isotope composition reflects the composition of the basement (i.e., Pb with isotopic composition similar to upper continental crust and the regional shale curve) as well as felsic and mafic volcanic rocks present in the Wolverine Basin (i.e., Pb from varying mixtures of juvenile [mantle derived] and upper crustal material). The Pb isotope apportionment of shales with mostly detrital material is shown as the left-hand column (i) in the lower half of the figure. This reflects the ambient upper crust with minor contamination from mafic and felsic detritus, and isotope compositions plot proximal to the shale curve in uranogenic Pb isotope space.

The deeply sourced hydrothermal fluid-associated Pb was leached from basement that comprised continental basement and felsic, mafic volcanic, and intrusive rocks. Additional Pb in the fluids could have come from deep magmatic volatiles. The Pb isotope apportionment of shales near VMS mineralization is shown in the middle column (ii). Lead from detritus was a minor source compared to the significant hydrothermal input that reflects varying contributions from crustal and juvenile Pb. In uranogenic Pb isotope space, these shales plot as an array between contemporaneous upper crust and juvenile sources. The influence of additional radiogenic Pb from seawater-derived U in these shales is negligible.

The shallow hydrothermal circulation of seawater into the Wolverine VMS system was poor in Pb (due to very low Pb concentration in seawater) but rich in oceanic nutrients (e.g., U, Mo). This caused carbonate alteration of affected shales and deposited U ($UO_2(CO_3)_3^{4+}$) that subsequently decayed to ^{206}Pb (and, to a lesser extent, ^{207}Pb). The Pb isotope apportionment of shales proximal to mineralization with dominant carbonate alteration is shown on the right-hand side panel. With time, U decay caused strong ^{206}Pb accumulation, resulting in a data array that plots significantly toward the right in uranogenic Pb isotope space (iii). The array of these samples also projects back toward the mineralized shale array, suggesting that, prior to U decay, they were similar to group (ii). DMM = depleted mid-ocean ridge basalt (MORB) mantle, SC = shale curve.

of hydrothermal input (e.g., chondritic Y/Ho, Zr/Hf, and no CO_2-U-metal enrichment).

The Pb isotope data for shales obtained in this study via Q-ICP-MS are sufficiently precise and accurate for the purpose of elucidating mineralization processes at the scale of entire districts. They benefit from concomitant analyses of high-precision trace element data from the same single digest (Kamber and Gladu, 2009). It is likely that Pb isotope data will become more readily available at lower cost in commercial laboratories in the coming years and their utility in mineral exploration will expand. In the Wolverine and similar basins and deposits globally, the combined deviation in $^{206,207,208}Pb/^{204}Pb$ toward lower values than local shale may become a potential exploration vector, if interpreted within the context of alteration mineralogy and trace element systematics.

Acknowledgments

This research has been financially and logistically supported by grants from Yukon Zinc Corporation, the Natural Sciences and Engineering Research Council of Canada (NSERC) Collaborative Research and Development program (Wolverine project), and NSERC Discovery Grants to Steve Piercey and Balz Kamber. This research project is also part of the Canadian Mining Industry Research Organization (CAMIRO) Project 08E04 on the Geochemistry of Shales as Vectors to Ore Deposits, funded by a consortium of companies and an NSERC Collaborative Research and Development Grant (CRDPJ-387591-09). Final preparation of this paper was undertaken while Piercey was a sabbatical visitor at Trinity College and the Irish Centre for Research in Applied Geology (iCRAG), and his residency there and this paper were made possible by a Dobbin Atlantic Scholarship from the Ireland Canada University Foundation (ICUF), provided with support from the Irish government. This research also represents a collaboration with iCRAG, which is funded by Science Foundation Ireland Grant Number 13/RC/2092, co-funded under the European Regional Development Fund. We are grateful for discussions and interactions with Geoff Bradshaw, Gilles Dessureau, Jason Dunning, Harold Gibson, Wayne Goodfellow, Graham Layne, Maribeth Moll, Dan Layton-Matthews, Don Murphy, and Jan Peter. Jim Mortensen is thanked for discussions about Pb isotopes and the "shale curve." They have shaped many of the views and arguments presented herein, but any errors or omissions are the responsibility of the authors. Thomas Ulrich, Annette Gladu, and Claire Kamber are thanked for their help and contributions to lab work at Laurentian University. Comments from reviewers Massimo Chiaradia and Sarah Gleeson helped sharpen and clarify many of our arguments, and greatly improved the quality of the final paper.

REFERENCES

Algeo, T.J., and Tribovillard, N., 2009, Environmental analysis of paleoceanographic systems based on molybdenum-uranium covariation: Chemical Geology, v. 268, p. 211–225.

Ayuso, R.A., and Schulz, K.J., 2003, Nd-Pb-Sr isotope geochemistry and origin of the Ordovician Bald Mountain and Mount Chase massive sulfide deposits, northern Maine: Economic Geology Monograph 11, p. 611–630.

Ayuso, R.A., Kelley, K.D., Leach, D.L., Young, L.E., Slack, J.F., Wandless, G., Lyon, A.M., and Dillingham, J.D., 2004, Origin of the Red Dog Zn-Pb-Ag deposits, Brooks Range, Alaska: Evidence from regional Pb and Sr isotope sources: Economic Geology, v. 99, p. 1533–1553.

Baker, J., Peate, D., Waight, T., and Meyzen, C., 2004, Pb isotopic analysis of standards and samples using a ^{207}Pb-^{204}Pb double spike and thallium to correct for mass bias with a double-focusing MC-ICP-MS: Chemical Geology, v. 211, p. 275–303.

Ballard, J., Palin, M., and Campbell, I., 2002, Relative oxidation states of magmas inferred from Ce(IV)/Ce(III) in zircon: Application to porphyry copper deposits of northern Chile: Contributions to Mineralogy and Petrology, v. 144, p. 347–364.

Bau, M., 1996, Controls on the fractionation of isovalent trace elements in magmatic and aqueous systems; evidence from Y/Ho, Zr/Hf, and lanthanide tetrad effect: Contributions to Mineralogy and Petrology, v. 123, p. 323–333.

Bau, M., and Dulski, P., 1999, Comparing yttrium and rare earths in hydrothermal fluids from the Mid-Atlantic Ridge; implications for Y and REE behaviour during near-vent mixing and for the Y/Ho ratio of Proterozoic seawater: Chemical Geology, v. 155, p. 77–90.

Bradshaw, G., 2003, Geology and genesis of the Wolverine polymetallic volcanic rock-hosted massive sulphide (VHMS) deposit, Finlayson Lake district, Yukon, Canada: M.Sc. thesis, Vancouver, University of British Columbia, 172 p.

Bradshaw, G.D., Rowins, S.M., Peter, J.M., and Taylor, B.E., 2008, Genesis of the Wolverine volcanic sediment-hosted massive sulfide deposit, Finlayson Lake district, Yukon, Canada: Mineralogical, mineral chemical, fluid inclusion, and sulfur isotope evidence: Economic Geology, v. 103, p. 35–60.

Collerson, K.D., and Kamber, B.S., 1999, Evolution of the continents and the atmosphere inferred from Th-U-Nb systematics of the depleted mantle: Science, v. 283, p. 1519–1522.

Collerson, K.D., Kamber, B.S., and Schoenberg, R., 2002, Applications of accurate, high-precision Pb isotope ratio measurement by multi-collector ICP-MS: Chemical Geology, v. 188, p. 65–83.

Creaser, R.A., Erdmer, P., Stevens, R.A., and Grant, S.L., 1997, Tectonic affinity of Nisutlin and Anvil assemblage strata from the Teslin Tectonic zone, northern Canadian Cordillera: Constraints from neodymium isotope and geochemical evidence: Tectonics, v. 16, p. 107–121.

Dahlkamp, F.J., 1993, Uranium ore deposits: Berlin, Springer-Verlag, 460 p.

David, K., Schiano, P., and Allegre, C.J., 2000, Assessment of the Zr/Hf fractionation in oceanic basalts and continental materials during petrogenetic processes: Earth and Planetary Science Letters, v. 178, p. 285–301.

Davies, R., Kennedy, J., McIlroy, R., Spence, R., and Hill, K., 1964, Extraction of uranium from sea water: Nature, v. 203, p. 1110–1115.

DeWolf, C.P., and Mezger, K., 1994, Lead isotope analyses of leached feldspars: Constraints on the early crustal history of the Grenville Orogen: Geochimica et Cosmochimica Acta, v. 58, p. 5537–5550.

Firdaus, M.L., Minami, T., Norisuye, K., and Sohrin, Y., 2011, Strong elemental fractionation of Zr-Hf and Nb-Ta across the Pacific Ocean: Nature Geoscience, v. 4, p. 227–230.

Franklin, J.M., and Thorpe, R.I., 1982, Comparative metallogeny of the Superior, Slave and Churchill provinces: Geological Association of Canada, Special Paper 25, p. 3–90.

Godwin, C.I., and Sinclair, A.J., 1982, Average lead isotope growth curve for shale-hosted zinc-lead deposits, Canadian Cordillera: Economic Geology, v. 77, p. 675–690.

Grant, S.L., 1997, Geochemical, radiogenic tracer isotopic, and U-Pb geochronological studies of Yukon-Tanana terrane rocks from the Money Klippe, southeastern Yukon, Canada: M.Sc. thesis, Edmonton, University of Alberta, 177 p.

Gulson, B.L., 1976, Exploration and mapping around a base metal sulphide deposit using trace lead isotopes: Mineralium Deposita, v. 11, p. 1–5.

——1986, Lead isotopes in mineral exploration: Amsterdam, Netherlands, Elsevier, 245 p.

Hannington, M.D., Galley, A.G., Herzig, P.M., and Petersen, S., 1998, Comparison of the TAG mound and stockwork complex with Cyprus-type massive sulfide deposits: Proceedings of the Ocean Drilling Program, Scientific Results, v. 158, p. 389–415.

Henderson, G.M., 2002, Seawater ($^{234}U/^{238}U$) during the last 800 thousand years: Earth and Planetary Science Letters, v. 199, p. 97–110.

Humphris, S.E., and Tivey, M.K., 2000, A synthesis of geological and geochemical investigations of the TAG hydrothermal field; insights into fluid-flow and mixing processes in a hydrothermal system: Geological Society of America, Special Paper 349, p. 213–235.

Kamber, B.S., 2009, Geochemical fingerprinting: 40 years of analytical development and real world applications: Applied Geochemistry, v. 24, p. 1074–1086.

Kamber, B.S., and Gladu, A.H., 2009, Comparison of Pb purification by anion-exchange resin methods and assessment of long-term reproducibility of Th/U/Pb ratio measurements by quadrupole ICP-MS: Geostandards and Geoanalytical Research, v. 33, p. 169–181.

Kamber, B.S., Webb, G.E., and Gallagher, M., 2014, The rare earth element signal in Archaean microbial carbonate: Information on ocean redox and biogenicity: Journal of the Geological Society, v. 171, p. 745–763.

Kodolányi, J., Pettke, T., Spandler, C., Kamber, B.S., and Gméling, K., 2011, Geochemistry of ocean floor and fore-arc serpentinites: Constraints on the ultramafic input to subduction zones: Journal of Petrology, v. 53, p. 235–270.

Kramers, J.D., and Tolstikhin, I.N., 1997, Two terrestrial lead isotope paradoxes, forward transport modelling, core formation and the history of the continental crust: Chemical Geology, v. 139, p. 75–110.

Layton-Matthews, D., Leybourne, M.I., Peter, J.M., Scott, S.D., Cousens, B., and Eglington, B.M., 2013, Multiple sources of selenium in ancient seafloor hydrothermal systems: Compositional and Se, S, and Pb isotopic evidence from volcanic-hosted and volcanic-sediment-hosted massive sulfide deposits of the Finlayson Lake district, Yukon, Canada: Geochimica et Cosmochimica Acta, v. 117, p. 313–331.

Linnen, R.L., and Keppler, H., 2002, Melt composition control of Zr/Hf fractionation in magmatic processes: Geochimica et Cosmochimica Acta, v. 66, p. 3293–3301.

Macfarlane, A.M., and Miller, M., 2007, Nuclear energy and uranium resources: Elements, v. 3, p. 185–192.

Marcoux, E., 1997, Lead isotope systematics of the giant massive sulphide deposits in the Iberian Pyrite Belt: Mineralium Deposita, v. 33, p. 45–58.

Marx, S.K., and Kamber, B.S., 2010, Trace-element systematics of sediments in the Murray-Darling Basin, Australia: Sediment provenance and palaeoclimate implications of fine scale chemical heterogeneity: Applied Geochemistry, v. 25, p. 1221–1237.

Mortensen, J.K., 1992, Pre-mid-Mesozoic tectonic evolution of the Yukon-Tanana terrane, Yukon and Alaska: Tectonics, v. 11, p. 836–853.

Mortensen, J.K., Dusel-Bacon, C., Hunt, J.A., and Gabites, J., 2006, Lead isotopic constraints on the metallogeny of middle and late Paleozoic syngenetic base metal occurrences in the Yukon-Tanana and Slide Mountain/Seventymile terranes and adjacent portions of the North American miogeocline: Geological Association of Canada, Special Paper 45, p. 261–279.

Mortensen, J.K., Hall, B.V., Bissig, T., Friedman, R.M., Danielson, T., Oliver, J., Rhys, D.A., Ross, K.V., and Gabites, J.E., 2008, Age and Paleotectonic setting of volcanogenic massive sulfide deposits in the Guerrero terrane of central Mexico: Constraints from U-Pb age and Pb isotope studies: Economic Geology, v. 103, p. 117–140.

Murphy, D.C., Mortensen, J.K., Piercey, S.J., Orchard, M.J., and Gehrels, G.E., 2006, Tectonostratigraphic evolution of Yukon-Tanana terrane, Finlayson Lake massive sulphide district, southeastern Yukon: Geological Association of Canada, Special Paper 45, p. 75–105.

Nelson, J.L., Colpron, M., Piercey, S.J., Murphy, D.C., Dusel-Bacon, C., and Roots, C.F., 2006, Paleozoic tectonic and metallogenetic evolution of pericratonic terranes in Yukon, northern British Columbia and eastern Alaska: Geological Association of Canada, Special Paper 45, p. 323–360.

Nozaki, Y., Zhang, J., and Amakawa, H., 1997, The fractionation between Y and Ho in the marine environment: Earth and Planetary Science Letters, v. 148, p. 329–340.

Peter, J.M., 2003, Ancient iron formations: Their genesis and use in the exploration for stratiform base metal sulphide deposits, with examples from the Bathurst mining camp: Geological Association of Canada, GEOtext, v. 4, p. 145–176.

Peter, J.M., Layton-Matthews, D., Piercey, S., Bradshaw, G., Paradis, S., and Boulton, A., 2007, Volcanic-hosted massive sulphide deposits of the Finlayson Lake district, Yukon: Geological Association of Canada, Mineral Deposits Division, Special Publication 5, p. 471–508.

Pettke, T., Kodolányi, J., and Kamber, B.S., 2018, From ocean to mantle: New evidence for U-cycling with implications for the HIMU source and the secular Pb isotope evolution of Earth's mantle: Lithos, v. 316, p. 66–76.

Piercey, S.J., and Colpron, M., 2009, Composition and provenance of the Snowcap assemblage, basement to the Yukon-Tanana terrane, northern Cordillera: Implications for Cordilleran crustal growth: Geosphere, v. 5, p. 439–464.

Piercey, S.J., Murphy, D.C., Mortensen, J.K., and Paradis, S., 2001a, Boninitic magmatism in a continental margin setting, Yukon-Tanana terrane, southeastern Yukon, Canada: Geology, v. 29, p. 731–734.

Piercey, S.J., Paradis, S., Murphy, D.C., and Mortensen, J.K., 2001b, Geochemistry and paleotectonic setting of felsic volcanic rocks in the Finlayson Lake volcanic-hosted massive sulfide district, Yukon, Canada: Economic Geology, v. 96, p. 1877–1905.

Piercey, S.J., Mortensen, J.K., and Creaser, R.A., 2003, Neodymium isotope geochemistry of felsic volcanic and intrusive rocks from the Yukon-Tanana terrane in the Finlayson Lake region, Yukon, Canada: Canadian Journal of Earth Sciences, v. 40, p. 77–97.

Piercey, S.J., Murphy, D.C., Mortensen, J.K., and Creaser, R.A., 2004, Mid-Paleozoic initiation of the northern Cordilleran marginal back-arc basin: Geological, geochemical and neodymium isotopic evidence from the oldest mafic magmatic rocks in Yukon-Tanana terrane, Finlayson Lake district, southeast Yukon, Canada: Geological Society of America Bulletin, v. 116, p. 1087–1106.

Piercey, S.J., Nelson, J.L., Colpron, M., Dusel-Bacon, C., Simard, R.-L., and Roots, C.F., 2006, Paleozoic magmatism and crustal recycling along the ancient Pacific margin of North America, northern Cordillera: Geological Association of Canada, Special Paper 45, p. 281–322.

Piercey, S.J., Peter, J.M., Mortensen, J.K., Paradis, S., Murphy, D.C., and Tucker, T.L., 2008, Petrology and U-Pb geochronology of footwall porphyritic rhyolites from the Wolverine volcanogenic massive sulfide deposit, Yukon, Canada: Implications for the genesis of massive sulfide deposits in continental margin environments: Economic Geology, v. 103, p. 5–33.

Piercey, S.J., Murphy, D.C., and Creaser, R.A., 2012, Lithosphere-asthenosphere mixing in a transform-dominated late Paleozoic backarc basin: Implications for northern Cordilleran crustal growth and assembly: Geosphere, v. 8, p. 716–739.

Piercey, S.J., Gibson, H.L., Tardif, N., and Kamber, B.S., 2016, Ambient redox and hydrothermal environment of the Wolverine volcanogenic massive sulfide deposit, Yukon: Insights from lithofacies and lithogeochemistry of Mississippian host shales: Economic Geology, v. 111, p. 1439–1463.

Piercey, S.J., Beranek, L.P., and Hanchar, J.M., 2017, Mapping magma prospectivity for Cordilleran volcanogenic massive sulphide (VMS) deposits using Nd-Hf isotopes: Preliminary results, *in* MacFarlane, K.E., and Weston, L.H., eds., Yukon exploration and geology 2016: Whitehorse, Yukon, Canada, Yukon Geological Survey, p. 197–205.

Plint, H.E., and Gordon, T.M., 1997, The Slide Mountain terrane and the structural evolution of the Finlayson Lake fault zone, southeastern Yukon: Canadian Journal of Earth Sciences, v. 34, p. 105–126.

Staudigel, H., Plank, T., White, B., and Schmincke, H.U., 1996, Geochemical fluxes during seafloor alteration of the basaltic upper oceanic crust: DSDP Sites 417 and 418: American Geophysical Union, Geophysical Monograph Series 96, p. 19–38.

Swinden, H.S., and Thorpe, R.I., 1984, Variations in style of volcanism and massive sulfide deposition in Early to Middle Ordovician island-arc sequences of the Newfoundland Central mobile belt: Economic Geology, v. 79, p. 1596–1619.

Thorpe, R.I., 1999, The Pb isotope linear array for volcanogenic massive sulfide deposits of the Abitibi and Waawa subprovinces, Canadian Shield: Economic Geology Monograph 10, p. 555–575.

Tivey, M.K., 2007, Generation of seafloor hydrothermal vent fluids and associated mineral deposits: Oceanography, v. 20, p. 50–65.

Tivey, M.K., Humphris, S.E., Thompson, G., Hannington, M.D., and Rona, P.A., 1995, Deducing patterns of fluid flow and mixing within the TAG active hydrothermal mound using mineralogical and geochemical data: Journal of Geophysical Research: Solid Earth, v. 100, p. 12,527–12,555.

Tosdal, R.M., Wooden, J.L., and Bouse, R.M., 1999, Pb isotopes, ore deposits, and metallogenic terranes: Reviews in Economic Geology, v. 12, p. 1–28.

Turner, E.C., and Kamber, B.S., 2012, Arctic Bay Formation, Borden Basin, Nunavut (Canada): Basin evolution, black shale, and dissolved metal systematics in the Mesoproterozoic ocean: Precambrian Research, v. 208–211, p. 1–18.

Ulrich, T., Kamber, B.S., Woodhead, J.D., and Spencer, L.A., 2010, Long-term observations of isotope ratio accuracy and reproducibility using quadrupole ICP-MS: Geostandards and Geoanalytical Research, v. 34, p. 161–174.

von Blanckenburg, F., O'Nions, R.K., and Heinz, J.R., 1996, Distribution and sources of pre-anthropogenic lead isotopes in deep ocean water from FeMn crusts: Geochimica et Cosmochimica Acta, v. 60, p. 4957–4963.

Zartman, R.E., and Doe, B.R., 1981, Plumbotectonics; the model: Tectonophysics, v. 75, p. 135–162.

Stephen Piercey obtained B.Sc. (Hons.) and M.Sc. degrees from Memorial University of Newfoundland and a Ph.D. from the University of British Columbia, and is currently a professor at Memorial University of Newfoundland. His research, teaching, and consulting interests are focused on field- and laboratory-based studies of VMS, orogenic Au, and U deposits with emphasis on understanding (1) tectonomagmatic settings of deposit formation; (2) reconstruction of their volcanic, sedimentary, and hydrothermal environments; (3) mineralogical, lithogeochemical, and hydrothermal footprint definition; and (4) the mineralogy and sources of metals, fluids, and sulfur in ore mineralization. He was the 2005 recipient of the Waldemar Lindgren Award.